Available online at www.sciencedirect.com

ScienceDirect

Geochimica et Cosmochimica Acta 142 (2014) 186–204

Geochimica et Cosmochimica Acta

www.elsevier.com/locate/gca

Diffusion kinetics of ^{3}He and ^{21}Ne in quartz and implications for cosmogenic noble gas paleothermometry

Marissa M. Tremblay [a,b,*], David L. Shuster [a,b], Greg Balco [b]

[a] Department of Earth and Planetary Science, University of California, Berkeley, 307 McCone Hall #4767, Berkeley, CA 94720-4767, USA
[b] Berkeley Geochronology Center, 2455 Ridge Road, Berkeley, CA 94709, USA

Received 24 February 2014; accepted in revised form 10 August 2014; Available online 20 August 2014

Abstract

The simultaneous production and diffusion of cosmogenic noble gases offers the potential to constrain past temperatures on Earth and other planetary surfaces. Knowledge of both the production rate and diffusion kinetics of cosmogenic nuclide pairs is required to utilize this open-system behavior for paleothermometry. Here, we investigate the diffusion kinetics of spallogenic ^{3}He and ^{21}Ne in quartz through a series of step-degassing experiments on individual, proton-irradiated quartz grains. Quartz often, but not always, exhibits two stages of linear Arrhenius behavior, with He and Ne exhibiting similar release patterns. This two-stage behavior does not appear to correlate with heating-induced structural changes or anisotropy, nor is it an artifact of proton irradiation. The behavior may instead be associated with a sample-specific property such as radiation damage, mineral inclusions, fluid inclusions, or structural defects. We interpret these two Arrhenius arrays to represent multiple diffusion domain (MDD)-type behavior in quartz, as two-domain models closely reproduce the experimental data. However, we are currently unable to link this behavior with a clear physical mechanism; a different, more mechanistic model may be more appropriate in future studies.

For both He and Ne, modeled Arrhenius diffusion parameters (activation energy, E_a, and pre-exponential factor, D_0) display a range of values in the quartz samples analyzed. For ^{3}He, E_a ranges from 73.0 to 99.8 kJ/mol and D_0 from 5.9×10^{0} to 1.0×10^{4} cm^2 s^{-1} for the initial, low-temperature linear Arrhenius arrays; when observed, a second array at higher temperatures corresponds to E_a ranging from 85.2 to 106.4 kJ/mol and D_0 from 1.7×10^{-1} to 3.5×10^{0} cm^2 s^{-1}. For ^{21}Ne, E_a ranges from 95.7 to 153.8 kJ/mol and D_0 from 6.6×10^{-1} to 3.2×10^{3} cm^2 s^{-1} for the initial, low-temperature array; linearity at high temperatures is not well constrained, likely because the α- to β-quartz transition occurs during the relevant temperature range. When extrapolated to Earth surface temperatures and geologically relevant timescales, these results suggest that 1 mm-radius quartz grains lose significant amounts of cosmogenic ^{3}He by diffusion at sub-zero temperatures from the low-retentivity domain over $>10^{3}$ yr timescales and from the high-retentivity domain over $>10^{4}$ yr, whereas quantitative retention of cosmogenic ^{21}Ne occurs over $>10^{6}$ yr at temperatures $\leqslant$40 °C in most cases. While these results are generally consistent with previously reported studies, they also reveal that sample-specific diffusion parameters are required for quantitative application of cosmogenic noble gas paleothermometry. The cosmogenic ^{3}He abundance in one quartz sample with a simple Holocene exposure history and the stepwise degassing pattern of cosmogenic ^{3}He and ^{21}Ne from another quartz sample with a ~1.2 Ma exposure history agree well with diffusion experiments on proton-irradiated aliquots of the same samples. For the sample with a simple Holocene exposure history, a production and diffusion model incorporating sample-specific diffusion parameters and the measured ^{3}He abundance predicts an effective diffusion temperature consistent with the effective modern temperature at the sample location. This internal consistency demonstrates that the empirically

* Corresponding author at: Department of Earth and Planetary Science, University of California, Berkeley, 307 McCone Hall #4767, Berkeley, CA 94720-4767, USA. Tel.: +1 603 203 4976.
E-mail addresses: mtremblay@berkeley.edu (M.M. Tremblay), dshuster@berkeley.edu (D.L. Shuster), balcs@bgc.org (G. Balco).

http://dx.doi.org/10.1016/j.gca.2014.08.010
0016-7037/© 2014 Elsevier Ltd. All rights reserved.

determined, sample-specific diffusion kinetics apply to cosmogenic ^{3}He and ^{21}Ne in quartz in natural settings over geologic timescales.
© 2014 Elsevier Ltd. All rights reserved.

1. INTRODUCTION

Cosmogenic nuclides, originating from nuclear interactions between secondary cosmic-ray particles and mineral targets in the outermost few meters of the solid Earth, are commonly used to estimate rates and times of geologic processes that modify the Earth's surface (Granger et al., 2013). The stable cosmogenic noble gases ^{3}He and ^{21}Ne have relatively high production rates in common minerals and are less expensive and less difficult to measure than cosmogenic radionuclides. However, early research into surface exposure dating showed that both ^{3}He and ^{21}Ne experience diffusive loss at Earth surface temperatures in quartz and feldspars, respectively (Cerling, 1990; Trull et al., 1991; Brook and Kurz, 1993; Brook et al., 1993; Shuster and Farley, 2005). These authors concluded that open-system behavior renders these cosmogenic noble gas–mineral pairs unfit for surface exposure dating, and they have not been used for this application. However, accurate knowledge of diffusion kinetics would overcome this limitation. In addition, these pairs may be useful as thermochronometers, recording integrated thermal histories of rocks during exposure within a few meters of the surface (Tremblay et al., 2014).

Utilizing this open-system behavior requires knowledge of both the production rate and diffusion kinetics of a particular cosmogenic nuclide-mineral pair. For quartz, the sea level high latitude (SLHL) production rate of cosmogenic ^{21}Ne in quartz has been quantified by geologic calibrations and artificial target experiments (e.g., Niedermann, 2000; Balco and Shuster, 2009; Kober et al., 2011). The production rate of cosmogenic ^{3}He in quartz is more difficult to empirically quantify from geological samples, given that existing estimates of He diffusion kinetics in quartz as well as comparison between measured concentrations of cosmogenic ^{3}He and other nuclides indicate diffusive loss at surface temperatures. However, the ^{3}He production rate in quartz can be estimated from production rates measured in other minerals combined with element-specific reaction cross-sections (Masarik and Reedy, 1995a,b; Ackert et al., 2011), and has also been directly measured in artificial target experiments (Vermeesch et al., 2009). Thus, production rates for these nuclides in quartz are reasonably well established. In contrast, relatively little work has studied mechanisms or kinetics of He and Ne diffusion in quartz.

A common method for quantifying noble gas diffusion kinetics involves step-degassing experiments on crystal fragments. In these experiments, samples are sequentially heated at controlled temperatures and durations, allowing a fraction of the gas present to diffuse from the solid in each heating step. The duration of, and gas fraction released in, each heating step can be used to calculate length scale-normalized diffusion coefficients, D/a^2, at each temperature (Fechtig and Kalbitzer, 1966). This method requires that: (1) diffusion is Fickian and isotropic (Crank, 1975), (2) the diffusant has a known initial distribution, and (3) the diffusion domain has fixed geometry. If the temperature dependence of diffusion follows an Arrhenius law, then the natural logarithm of the calculated diffusivities $\ln(D/a^2)$ will correlate linearly with inverse absolute temperature. The diffusion parameters of activation energy, E_a, and pre-exponential factor, D_0, can be quantified from the slope and y-intercept, respectively, of a linear regression through an Arrhenius array, and given the further assumption of Arrhenius behavior at all temperatures then used to calculate diffusivity at any temperature. Noble gas diffusion kinetics have also been quantified by inward diffusion experiments (e.g., Watson and Cherniak, 2003; Cherniak et al., 2014) and implantation experiments (Cherniak et al., 2009, 2014). These experiments are fundamentally different from step-degassing experiments because they occur over extremely small distances (hundreds of nm) and can thus avoid sample heterogeneities like defects and inclusions. Geologic applications of cosmogenic noble gas measurements, however, requires quantifying noble gas diffusion across the grain scale of natural samples, which often include such heterogeneities. Degassing experiments provide an empirical quantification that includes such complexity and are thus employed here.

To our knowledge, only two published sets of step-degassing experiments fully quantify the diffusion kinetics of ^{3}He and ^{21}Ne in quartz. Trull et al. (1991) measured diffusivities of cosmogenic ^{3}He in quartz that indicate quantitative retention of ^{3}He in large (>2 mm) quartz grains on 10^{6} yr timescales. Using aliquots of gem-quality quartz containing a uniform distribution of proton-induced ^{3}He and ^{21}Ne, Shuster and Farley (2005) measured diffusion kinetics that predict quartz grains with diameters >1 mm will retain Ne at most Earth surface temperatures but will experience significant diffusive loss of He at subzero temperatures on $>10^{2}$–10^{3} yr timescales. Their results also suggest that the Trull et al. (1991) experiments may have been compromised by partial diffusive loss of cosmogenic ^{3}He. However, it is unclear whether noble gas diffusion kinetics in gem-quality quartz is applicable to commonly occurring quartz with variable physical characteristics. For example, Niedermann et al. (1993) estimated an activation energy for ^{21}Ne diffusion in quartz that is significantly lower than that determined by Shuster and Farley (2005). Similarly, Trull et al. (1995) observed that late-Pleistocene and Holocene-aged quartz samples from Death Valley, California, despite some of the highest surface temperatures on Earth, retain significantly more cosmogenic ^{3}He than expected from the diffusion parameters of Shuster and Farley (2005). These observations indicate that the diffusion kinetics of ^{3}He and ^{21}Ne may vary significantly amongst natural quartz samples.

Here we investigate the diffusion kinetics of ^{3}He and ^{21}Ne in quartz through degassing experiments on a suite of proton-irradiated fragments of natural quartz samples. Using the range of observed diffusion parameters, we model how concentrations of cosmogenic ^{3}He and ^{21}Ne evolve as a function of exposure duration and temperature at the Earth's surface and explore how retention of both cosmogenic nuclides can vary amongst different quartz samples. We also pair the proton-induced ^{3}He and ^{21}Ne experiments with measurements of cosmogenic ^{3}He and ^{21}Ne abundances to evaluate whether the diffusion kinetics observed in the laboratory accurately quantify temperature records integrated over a sample's cosmogenic exposure history.

2. METHODS

2.1. Proton irradiation

To quantify the variability of He and Ne diffusion kinetics in quartz, we conducted step-degassing experiments on a suite of quartz samples, originally collected for cosmogenic exposure dating, that span a range of petrologic origins and geologic histories. Sample descriptions are provided in Table 1; photographs of the quartz fragments used in diffusion experiments are shown in Fig. S1. Step-degassing experiments require a measurable abundance and known distribution of the diffusant at the start of the experiment. To achieve this, we irradiate our samples with energetic protons, which generates uniform distributions of ^{3}He and ^{21}Ne in quartz through similar nuclear transmutations as those induced by cosmic rays but with at least ten orders of magnitude higher production rates (Shuster and Farley, 2005; Shuster et al., 2004). Aliquots of quartz samples were irradiated with a ~220 MeV proton beam for ~5 h at the Francis H. Burr Proton Therapy Center at the Massachusetts General Hospital (Shuster et al., 2004). Samples CarBZ and UB09-4 were irradiated in April 2013 with a total fluence of $\sim 8.5 \times 10^{15}$ p/cm^2; all other samples were irradiated in April 2011 with a total fluence of $\sim 1.0 \times 10^{16}$ p/cm^2. As we show later, the abundance of cosmogenic ^{21}Ne and ^{3}He in some natural samples that have experienced exceptionally long (e.g., millions of years) exposure durations can be high enough to support step-degassing experiments on multi-grain quartz aliquots. However, the much higher abundance attainable by proton irradiation (at least three orders of magnitude greater than non-proton induced components) permits more detailed and more precise measurements on single quartz grains, which reduces complications caused by variation in grain size, shape, and other properties. Additionally, and more importantly for ^{3}He, our existing knowledge of diffusion kinetics predicts that cosmogenic ^{3}He in naturally irradiated quartz will in most cases have a nonuniform and unknown distribution due to diffusive loss at Earth surface temperatures and will therefore be unsuitable for step-degassing experiments.

2.2. Stepwise heating and degassing experiments

We screened irradiated quartz aliquots under an optical microscope for large fractures, mineral inclusions, and fluid inclusions. We chose quartz fragments apparently lacking these features and photographed and measured each fragment from multiple sides using a calibrated petrographic microscope (Fig. S1). Selected fragments were loaded into Pt–Ir alloy envelopes attached to K-type thermocouples and put under vacuum. Either a 30 W or 70 W diode laser was used to heat each sample, with the laser beam defocused over the Pt–Ir envelope to ensure uniform heating. The thermocouple and laser are connected in a feedback loop with a PID temperature controller, which allows the Pt–Ir envelope temperature to be regulated and measured to within ~2 °C.

Each sample was heated over at least fifty consecutive heating steps, including at least two retrograde heating

Table 1
Description of quartz samples studied in diffusion experiments.

Sample name	Description	Apparent exposure age
03-RDY-011-QZH	Ice-transported granitic boulder, Transantarctic Mountains	>4.9 ± 1.1 Ma (^{10}Be)[a] 10.6 ± 0.2 Ma (^{21}Ne)[b]
04-MG-080-BR	Quartzofeldspathic gneiss bedrock, Antarctic Dry Valleys	248 ± 27 ka (^{10}Be) 220 ± 25 ka (^{26}Al)
04-RDY-139-STR	Vein quartz boulder, Transantarctic Mountains	0.60 ± 0.04 Ma (^{10}Be) 1.188 ± 0.072 Ma (^{21}Ne)
98-PCM-105-MNZ	Quartzofeldspathic erratic boulder, Mt. Menzies massif, East Antarctica	>5.11 ± 1.24 Ma (^{10}Be) 8.76 ± 0.35 Ma (^{21}Ne)
CarBZ	Gem-quality quartz, Luis Serra do Ouro Mine, Serra Pelada, Carajas, Brazil	—
HU-08-03	Moraine boulder of Miocene welded rhyolite tuff, Huancané Valley, Peru	12.35 + 0.2/−0.02 ka (^{14}C, ^{10}Be)[c,d]
QA-767-Q	Phenocryst-rich trachyte, upper part of the Ammonia Tanks Tuff, Yucca Mountain, Nevada USA	605 ± 18 ka (^{21}Ne)[b]
UB09-4	Phreatic eruption ejecta cobble of felsic granitoid, Ubehebe volcanic field, Death Valley, California USA	3.3 ± 0 ka (^{10}Be)[e]

[a] Bromley et al. (2010).
[b] Gourbet et al. (2012).
[c] Kelly et al. (2012).
[d] Kelly et al. (2013).
[e] Sasnett et al. (2012).

cycles, to temperatures between 70 and 1200–1250 °C, with each step lasting 0.25–3 h. The released gas was purified in an automated, pneumatically-controlled extraction system under ultra high vacuum with a SAES® GP-50 getter pump fitted with C-50 cartridge (St101 alloy), brought to 11 K on temperature-controlled cryogenic trap, and then heated to 33 K and 70 K to release helium and neon, respectively. Each element was measured separately with an MAP 215-50 sector field mass spectrometer using a single, continuous dynode electron multiplier in pulse counting mode in the BGC Noble Gas Thermochronometry Lab. Each purified gas was analyzed under static vacuum conditions; time zero intercepts (and standard deviations) from linear regressions of the measurements of each nuclide over the course of ~1 h provided the raw signal (and its uncertainty). Between six and ten room temperature procedural blanks were periodically measured during each experiment and subtracted from the raw signals; the average magnitude of blank corrections was 0.14×10^6 atoms for ^{3}He, 37×10^6 atoms for ^{4}He, and 0.13×10^6 atoms for ^{21}Ne. Aliquots of a manometrically-calibrated air standard were also analyzed after approximately every fifth heating step using the same purification procedure described above and used to determine helium and neon sensitivities of the mass spectrometer. These sensitivities were constant over the pressure range of the analyses, as determined by measuring a series of different calibrated pipette volumes of the air standard. Measured isotopic compositions of helium and neon in this standard were indistinguishable from atmospheric. Following the diffusion experiment, each sample was removed from its Pt–Ir packet to examine whether the grain broke during the experiment, re-photographed, and then heated to 1250 °C in a laser chamber to ensure complete degassing. Blank-corrected ^{3}He, ^{21}Ne, and ^{4}He/^{3}He measurements from each experimental heating step are reported in Table S1; no isobaric interference corrections were necessary. We used the measured release fraction and duration of each heating step to calculate diffusion coefficients using the equations of Fechtig and Kalbitzer (1966) as discussed above, assuming that the quartz diffusion domain is represented by the whole crystal fragment and is spherical. The assumption of a spherical geometry is appropriate for fragments with modest aspect ratios if the surface area to volume ratio of the actual diffusion domain and the spherical approximation are equivalent (Meesters and Dunai, 2002; Farley et al., 2010), which we determined from our petrographic microscope measurements.

2.3. Cosmogenic ^{3}He and ^{21}Ne measurements

In addition to experiments on proton-irradiated quartz, we performed a similar step-degassing experiment on a non-irradiated aliquot of the Antarctic vein quartz sample 04-RDY-139-STR. This sample is from a high-elevation site in the Transantarctic Mountains (86.50171° S, 124.48661° E, 2356 masl) with a very low erosion rate and therefore has unusually high natural concentrations of cosmogenic ^{21}Ne and ^{3}He. The precise exposure history of this sample is unknown and, based on cosmogenic ^{26}Al and ^{10}Be concentrations, most likely includes multiple periods of exposure and burial. We measured bulk concentrations of ^{20}Ne, ^{21}Ne, and ^{22}Ne in this sample using the method described in Balco and Shuster (2009) and found a total ^{21}Ne concentration of 288.2 ± 3.5 Matoms/g. Ne isotope ratios in three heating steps were indistinguishable from the atmospheric-cosmogenic mixing line (Niedermann et al., 1993, 1994), and the assumption of two-component mixing implies that the sample contains 199.1 ± 3.7 Matoms/g cosmogenic ^{21}Ne and 89.0 ± 3.8 Matoms/g ^{21}Ne attributable to trapped Ne with atmospheric composition (Table S2, Fig. S2). This concentration of cosmogenic ^{21}Ne implies an apparent exposure age of ~1.25 Ma. From a crushed but otherwise unprocessed fraction of this sample that had been stored at room temperature since collection in 2004, we picked 0.0753 g of quartz fragments (~100 grains) similar in size to the proton-irradiated grain analyzed in the single-grain step-degassing experiment. We sequentially heated and degassed this multi-grain aliquot following the same procedure as described in Section 3.2, but loaded the sample into a large tantalum packet rather than the small Pt–Ir packets used for single grain experiments on proton-irradiated quartz. We then compared calculated D/a^2 values from the proton-irradiated and cosmogenic experiments to test whether the diffusion kinetics of proton-induced ^{3}He and ^{21}Ne are consistent with the observed degassing profiles of cosmogenic ^{3}He and ^{21}Ne. Blank-corrected ^{3}He and ^{21}Ne measurements from each heating step in this experiment are reported in Table S3. ^{20}Ne and ^{22}Ne signals in individual heating steps were too low to permit accurate Ne isotope ratio measurements due to isobaric interferences (Niedermann et al., 1993) and are therefore not reported.

We also tested whether the diffusion kinetics determined from our experimental results are representative of natural geologic conditions by measuring bulk cosmogenic ^{3}He abundances in six aliquots of quartz from sample HU-08-03. HU-08-03 was collected from a boulder of rhyolitic ignimbrite on the Huancane IIa moraine of the Quelccaya Ice Cap in Peru (13.9461° S, 70.8927° W, 4862 masl; Kelly et al., 2012, 2013) for cosmogenic-nuclide production rate calibration during the CRONUS-Earth project. This moraine is radiocarbon-dated at 12,350 cal yr BP (Kelly et al., 2012). Geological evidence and concentrations of other cosmic-ray-produced radionuclides indicates that the sample was emplaced at this time and subsequently experienced a single period of exposure at its present location (Kelly et al., 2013). As with sample 04-RDY-139-STR discussed above, we separated quartz from a fraction of this sample that had been crushed but not otherwise processed, and had been stored at room temperature since collection. Quartz aliquots of 100–200 mg were packaged in tantalum packets, placed under vacuum in a sample chamber, and heated with a 70 W diode laser to either 700 or 1200 °C for 1 h. Repeat extractions at either temperature yielded He signals indistinguishable from blank measurements. We analyzed the helium released during heating according to the techniques described in Section 3.2. However, these analyses released large quantities of ^{4}He in addition to ^{3}He, which resulted in the total He pressure in the mass spectrometer being outside the calibration range attainable with available standard gas pipettes. To account for this, we

introduced a ^{3}He spike into the mass spectrometer after several peak-hopping measurement cycles and used the difference in ^{3}He signals at the time of spike inlet between samples and standards to correct for nonlinearity. Having corrected for nonlinearity in this way, we then applied a blank correction as described above. We propagated (sometimes large) uncertainties associated with both nonlinearity and blank corrections, and averaged results from six aliquots to estimate the total ^{3}He concentration. In order to evaluate this ^{3}He concentration in the context of this sample's known exposure age (Kelly et al., 2013), we assume that all ^{3}He is cosmogenic.

2.4. Sample characterization

Numerous factors can lead to variable diffusion kinetics and complex Arrhenius diffusive behavior for a given mineral-diffusant pair, including anisotropy (e.g., Reich et al., 2007), temperature-induced structural transformations (e.g., Cassata and Renne, 2013), accumulation of radiation damage (e.g., Shuster et al., 2006; Flowers et al., 2009; Guenthner et al., 2013), the presence of mineral and/or fluid inclusions (e.g., Watson and Cherniak, 2003), and crystallographic defects (e.g., Saadoune et al., 2009; Baxter, 2010). The effects of the former three factors can be determined or at least approximated based on the results from diffusion experiments. We carried out several ancillary analyses in order to evaluate whether the latter two factors influenced the diffusion kinetics observed in our samples.

Although very large fluid and mineral inclusions readily visible under the binocular microscope were avoided, smaller ($\leqslant$20 μm) inclusions were difficult to recognize by visual inspection in the relatively large quartz fragments with pronounced conchoidal fracturing chosen for experiments. We made grain mounts of 20–50 quartz fragments from each sample and examined the mounts both on an optical petrographic microscope and a Zeiss EVO scanning electron microscope (SEM) in backscattering mode in order to characterize the relative abundances and types of inclusions characteristic of each sample.

To evaluate whether the observed diffusion kinetics relate to crystallographic defects and/or mineral and fluid inclusions, we also measured the concentrations of several trace elements in our samples. Crystallographic point defects and dislocations in quartz are often associated with the presence of trace elements, which can both substitute for silicon in the structural configuration or interstitially occupy *c*-axis channels (e.g., Müller et al., 2003; Götze et al., 2004). For example, Al^{3+} commonly substitutes for structural Si^{4+}, and an alkali metal like Li^+, Na^+, or K^+ occupies the adjacent interstice for charge compensation, creating an $[AlO_4^-|M^+]^0$ point defect (e.g., Dennen, 1966; Weil, 1992; Müller et al., 2003). Although less common, Fe^{3+} and Ti^{4+} also substitute for Si^{4+} in quartz. Mineral and fluid inclusions in quartz can also contain significant concentrations of Na and K as well as Ca, Mg, and Mn (Götze et al., 2004). To measure trace element concentrations, we dissolved several-hundred-milligram aliquots of quartz from each sample in hydrofluoric acid. We added a small amount of 1% sulfuric acid to each sample solution and then heated the solutions to remove Si by evaporating SiF_4 while keeping the elements of interest in solution. We then diluted each sample to achieve a 1% HNO_3, 1% H_2SO_4 solution for analysis. Bracketing standard solutions containing Al, Ca, Fe, K, Li, Mg, Mn, Na, and Ti were made with the same matrix (1% HNO_3, 1% H_2SO_4), and sample concentrations were measured by comparison with these standard solutions on a Perkin Elmer 5300 DV inductively coupled plasma optical emission spectrometer (ICP-OES) in the College of Natural Resources at UC Berkeley.

3. RESULTS

3.1. Step-degassing experiments on proton-irradiated quartz

Arrhenius plots are shown for step-degassing experiments on proton-irradiated fragments of HU-08-03 (Fig. 1), QA-767-Q(1) (Fig. 2), and UB09-4 (Fig. 3). These three experiments span the range of observed Arrhenius behavior and diffusion parameters; Arrhenius plots for all experiments, including a replicate experiment on sample QA-767-Q, are shown in the Supplementary materials (Figs. S3–S8). The equations of Fechtig and Kalbitzer (1966) use the cumulative gas release fraction to calculate diffusivities. However, linear propagation of uncertainties in cumulative gas release fraction from our step heating experiments would result in unrealistically large uncertainties in diffusivities. To address this, uncertainties in the calculated diffusivities of ^{3}He and ^{21}Ne for each heating step were propagated using a Monte Carlo approach, whereby we generated 30,000 normally distributed, random datasets using the analytical uncertainties in measured ^{3}He and ^{21}Ne to calculate a range of permissible D/a^2 values. We fit least squares regressions through a subset of the data points in each Arrhenius plot (see below) and used the Monte Carlo-derived uncertainties in D/a^2 to estimate uncertainties in E_a and $\ln(D_0/a^2)$ for both ^{3}He and ^{21}Ne. We also plot the residuals, or differences between the calculated diffusivity of ^{3}He and ^{21}Ne at each heating step and the expected diffusivity at the same temperature from the Arrhenius linear regressions, as a function of temperature (Figs. 1B–3B) and cumulative release fraction (Figs. 1C–3C).

Simple, linear Arrhenius behavior was not observed in most experiments. Instead, two linear Arrhenius arrays were observed for both ^{3}He and ^{21}Ne in six of the nine step-degassing experiments: one at lower temperatures and one at higher temperatures, separated by a transition zone where diffusivity changes relatively little with increasing temperature (Figs. 1A and 2A). When fitting least squares regressions, we followed an approach similar to those of Gourbet et al. (2012) and Cassata and Renne (2013). Our objective was to include data from as many temperature steps as possible that make up a linear Arrhenius array while minimizing the residuals (e.g., Fig. 1B–C) between the regression and the data. We typically excluded prograde steps with residuals $\geqslant 1\ \ln(s^{-1})$ from the least squares regression through the preceding sequential steps and retrograde steps with residuals $\geqslant 2\ \ln(s^{-1})$ from the least squares regression through the preceding and following prograde steps. For ^{3}He, the first few temperature steps

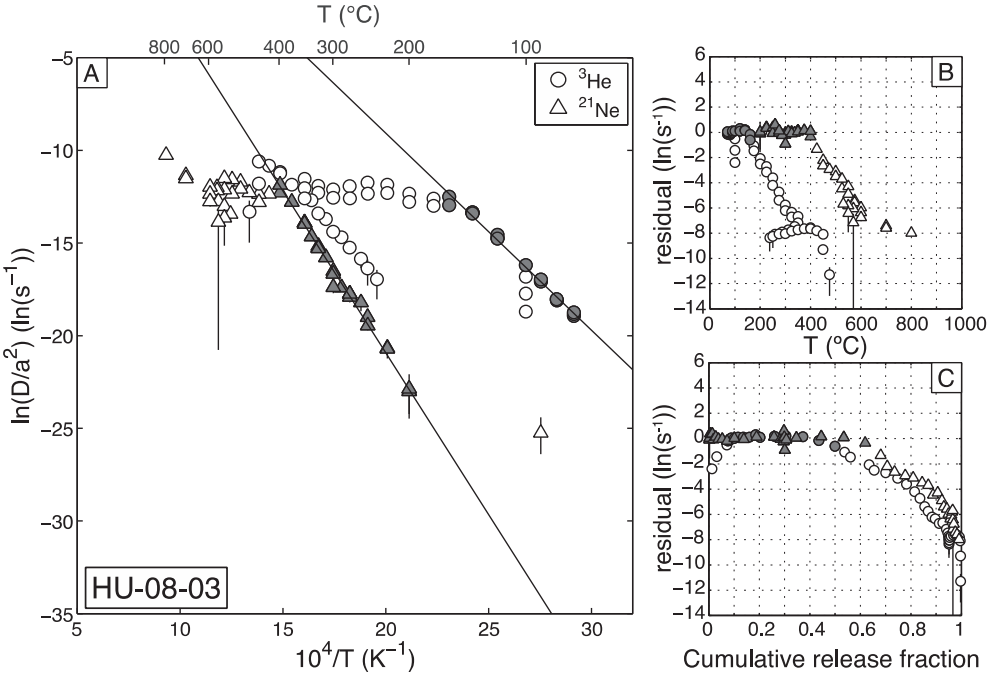

Fig. 1. Arrhenius plot (A) and residual plots (B–C) for diffusion of proton-induced ^{3}He (circles) and ^{21}Ne (triangles) in quartz from sample HU-08-03, a rhyolitic moraine boulder from Peru. Calculated uncertainties in $\ln(D/a^2)$ for each temperature step are shown, although in most cases the uncertainty is smaller than the symbol. Uncertainties in $\ln(D/a^2)$ were estimated using a Monte Carlo approach (see text). Linear regressions were fit through the filled symbols in (A) and used to calculate E_a and $\ln(D_0/a^2)$, with uncertainties propagated from the Monte Carlo scheme. The difference between the $\ln(D/a^2)$ calculated for each heating step and that predicted by the linear regression is plotted as a residual against temperature (B) and cumulative release fraction (C). Filled symbols correspond to those in (A).

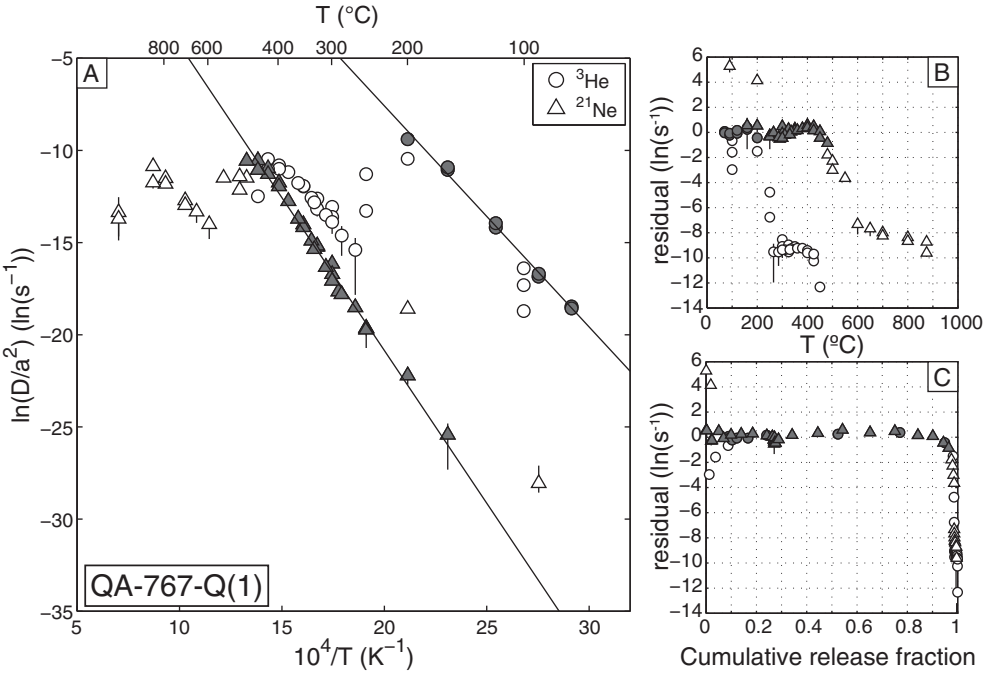

Fig. 2. Arrhenius plot (A) and residual plots (B–C) for diffusion of proton-induced ^{3}He (circles) and ^{21}Ne (triangles) in quartz from sample QA-767-Q(1) of the Ammonia Tanks Tuff, Yucca Mountain USA.

at 100 °C, which represent ⩽9% of the total ^{3}He yield, exhibit increasing apparent diffusivities. This is likely due to minor diffusive loss of ^{3}He either during or after the proton irradiation (Shuster and Farley, 2005); to minimize potential bias from this effect, we also exclude these steps from the regressions. The linear Arrhenius arrays and transition

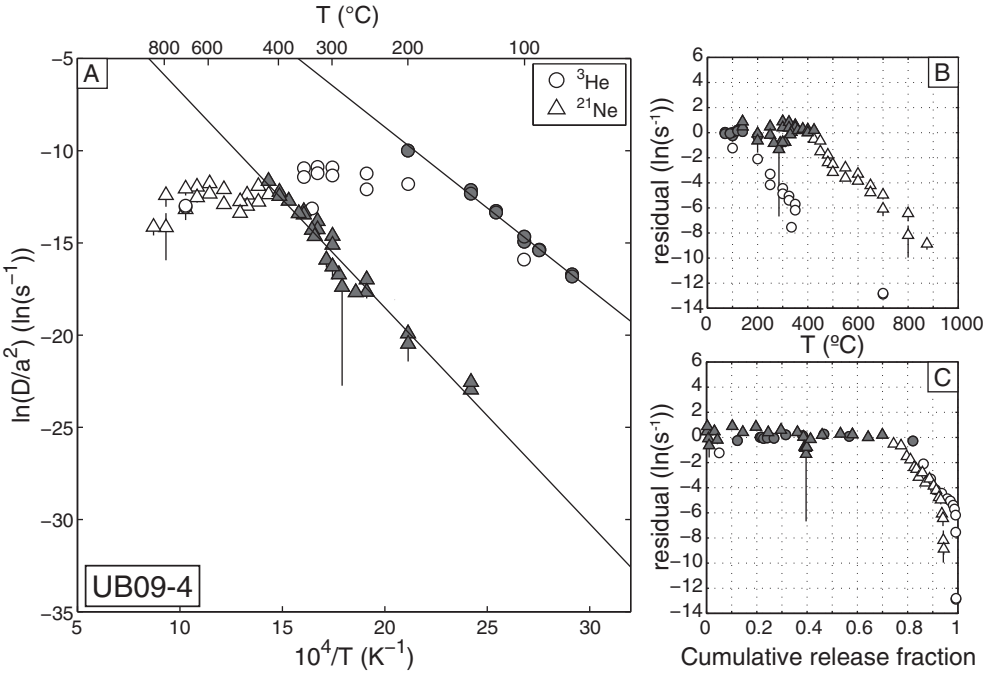

Fig. 3. Arrhenius plot (A) and residual plots (B–C) for diffusion of proton-induced ^{3}He (circles) and ^{21}Ne (triangles) in quartz from sample UB09-4, a felsic granitoid ejecta cobble from a phreatic eruption in the Ubehebe volcanic field, Death Valley, California USA.

zones occur over different temperature ranges for ^{3}He and ^{21}Ne (Figs. 1B–2B). However, with the exception of sample 04-MG-080-BR, the cumulative gas release fractions comprising the low-temperature linear arrays in each experiment are nearly equivalent for ^{3}He and ^{21}Ne (Figs. 1C–2C); in other words, divergence from the low-temperature linear arrays occur at the same gas release fraction, but not the same temperature, for He and Ne. Between different quartz samples, the proportion of ^{3}He and ^{21}Ne within the low-temperature linear arrays varies greatly, ranging from ~50% for HU-08-03 (Fig. 1C) to >95% for QA-767-Q(1) (Fig. 2C). Likewise, plots of the residuals versus temperature for HU-08-03 (Fig. 1B) and QA-767-Q(1) (Fig. 2B) reveal that the temperatures ranges over which we observed linear Arrhenius behavior of ^{3}He and ^{21}Ne vary between samples. Higher-temperature linear Arrhenius arrays are well defined for ^{3}He and represent as much as 20% of the cumulative gas release fraction. We report calculated diffusion parameters and sample dimensions for all experiments in Table 2, and include E_a and $\ln(D_0/a^2)$ estimates for these second linear arrays when observed. We report a second set of ^{21}Ne diffusion kinetic parameters for three of these experiments in which the proportions of ^{3}He and ^{21}Ne in the higher temperature linear Arrhenius arrays are equivalent (Table 2).

We did not observe a second linear Arrhenius array at higher temperatures in the experiment on sample UB09-4 (Fig. 3). More than 80% of the ^{3}He and ^{21}Ne released in the UB09-4 experiment makes up a linear Arrhenius array, with the remaining <20% deviating from the linear trend (Fig. 3A, C). We also did not observe second linear Arrhenius arrays in experiments on quartz from 03-RDY-011-QZH (Fig. S3) and CarBZ (Fig. S7). Like UB09-4, <60% of the gas released from CarBZ makes up a linear Arrhenius array at low temperatures, while >95% of the gas released in the experiment on 03-RDY-011-QZH makes up a single linear Arrhenius array. The activation energies of ^{3}He and ^{21}Ne diffusion calculated for these three samples are in several cases significantly lower than those calculated for the first linear Arrhenius array in experiments where two arrays were observed. To summarize, we observed two well-defined Arrhenius arrays in the He data from six of our nine experiments; in the other three experiments, a second Arrhenius array was not observed. For the Ne data, we observed two distinct arrays in only three experiments. When we observed two well-defined arrays in the Ne data we also observed two arrays in the He data, but the reverse is not the case.

Fig. 4 shows the range of Arrhenius relationships we observed for ^{3}He and ^{21}Ne, both for the low-temperature linear arrays and for the high-temperature linear arrays when observed. For the low-temperature arrays, ^{3}He activation energies range from 73.0 to 99.8 kJ/mol and the pre-exponential factor, D_0, ranges from 5.9×10^0 to 1.0×10^4 cm^2 s^{-1}. When observed, the second linear array at higher temperatures corresponds to ^{3}He activation energies ranging from 85.2 to 106.4 kJ/mol and D_0 values ranging from 1.7×10^{-1} to 3.5×10^0 cm^2 s^{-1}. In most experiments, the activation energies calculated for these second arrays are indistinguishable within uncertainty from the activation energy calculated from the low-temperature arrays. ^{21}Ne activation energies range from 95.7 to 153.8 kJ/mol and D_0 values range from 6.6×10^{-1} to 3.2×10^3 cm^2 s^{-1} for the low-temperature array. For the three experiments comprising equivalent release fractions for ^{3}He and ^{21}Ne in the high-temperature linear arrays,

Table 2
Summary of ^{3}He and ^{21}Ne quartz diffusion parameters. 1σ uncertainties are reported.

Sample	SR[a] (μm)	^{3}He, low-temperature array[b]				^{3}He, high-temperature array[c]			
		E_a (kJ/mol)	(±)	ln(D_0/a^2) (ln(s^{-1}))	(±)	E_a (kJ/mol)	(±)	ln(D_0/a^2) (ln(s^{-1}))	(±)
03.RDY.011.QZH	252	96.3	2.3	15.4	0.6	—	—	—	—
04-MG-080-BR	328	95.4	1.0	12.8	0.3	92	17	5.8	3.6
04-RDY-139-STR	426	96.6	0.7	13.8	0.2	93.0	1.9	5.9	0.4
98-PCM-105-MNZ	349	97.5	0.6	15.1	0.2	90.9	7.4	5.1	1.6
CarBZ	388	75.3	0.6	9.6	0.2	—	—	—	—
HU-08-03	256	88.5	1.1	12.2	0.3	98.8	6.6	6.4	1.6
QA-767-Q (1)	280	99.8	2.1	16.4	0.6	106.4	13.4	8.4	3.5
QA-767-Q (2)	306	99.6	0.4	15.2	0.1	85.2	16.6	5.2	4.7
UB09-4	299	73.0	0.8	8.8	0.2	—	—	—	—
		^{21}Ne, low-temperature array[b]				^{21}Ne, high-temperature array[c]			
		E_a (kJ/mol)	(±)	ln(D_0/a^2) (ln(s^{-1}))	(±)	E_a (kJ/mol)	(±)	ln(D_0/a^2) (ln(s^{-1}))	(±)
03.RDY.011.QZH	252	101.9	7.4	6.3	1.5	—	—	—	—
04-MG-080-BR	328	136.6	12.5	14.9	3.0	—	—	—	—
04-RDY-139-STR	426	107.7	4.0	5.9	0.8	126.8	2.4	6.0	0.3
		121.8	6.6	9.8	1.4				
98-PCM-105-MNZ	349	116.5	4.5	8.4	0.9	—	—	—	—
		121.3	5.6	9.9	1.2				
CarBZ	388	143.9	3.3	14.1	0.7	—	—	—	—
HU-08-03	256	145.2	8.3	14.0	1.7	90.6	9.7	−0.1	1.2
QA-767-Q (1)	280	139.9	4.9	12.8	0.9	89.4	17.6	−1.8	2.0
QA-767-Q (2)	306	153.8	6.5	16.6	1.3	—	—	—	—
UB09-4	299	95.7	1.9	4.5	0.4	—	—	—	—

[a] Radius of a sphere with a surface to volume ratio approximately equal to that of the quartz analyzed based on measured cross-dimensions of each quartz fragment. Images of proton-irradiated quartz fragments are shown in Fig. S1.

[b] In cases where two linear Arrhenius arrays were observed during an experiment, these values correspond to the linear Arrhenius array observed at lower temperatures. For 04.RDY.139.STR and 98.PCM.105.MNZ, we report two sets of ^{21}Ne diffusion kinetics. The first set of diffusion kinetics corresponds to the largest subset of ^{21}Ne data that forms a low-temperature linear array. The second set of diffusion kinetics corresponds to a smaller subset of the ^{21}Ne data that forms a low-temperature linear array with a better linear fit. Filled data points in Figs. S5 and S6 were used to calculate the first set of diffusion kinetics.

[c] If observed, these values correspond to the linear Arrhenius array observed at higher temperatures. For ^{21}Ne, diffusion parameters are only shown for the high-temperature linear array if the ^{21}Ne release fraction is equivalent to the release fraction of ^{3}He making up a high temperature linear array in the same experiment.

^{21}Ne activation energies range from 89.4 to 126.8 kJ/mol and D_0 values range from 5.9×10^{-4} to 7.3×10^{-1} cm^2 s^{-1}. For two of these three cases, the activation energies calculated from the high-temperature ^{21}Ne array are inconsistent with those calculated from the low-temperature array. The Arrhenius relationships for ^{3}He and ^{21}Ne reported by Shuster and Farley (2005) and for ^{3}He reported by Trull et al. (1991) are also plotted in Fig. 4 for comparison. The simple Arrhenius relationships for ^{3}He and ^{21}Ne calculated by Shuster and Farley (2005) from step-degassing experiments on gem-quality quartz fall within the range of Arrhenius relationships characterized by the low-temperature linear arrays in our experiments. The single linear Arrhenius array observed by Trull et al. (1991) is very close to the range linear ^{3}He arrays we observed at higher temperatures.

3.2. Natural cosmogenic ^{3}He and ^{21}Ne measurements

We observed two linear Arrhenius arrays in the step-degassing experiment carried out on a proton-irradiated fragment of vein quartz sample 04-RDY-139-STR (Fig. S5). Fig. 5 shows the results of a step-degassing experiment on an unirradiated, multi-grain quartz aliquot from sample 04-RDY-139-STR, with the results of the proton-irradiated step-degassing experiment plotted for comparison. The calculated diffusivities of cosmogenic ^{3}He at low-temperature heating steps (85% of the total cosmogenic ^{3}He) are significantly lower than those of proton-induced ^{3}He diffusivities at the same temperatures. In contrast, we observed close agreement between cosmogenic and proton-induced ^{3}He diffusivities at the end of the transition zone and throughout the second, higher temperature linear Arrhenius array observed for proton-induced ^{3}He (Fig. 5A).

Cosmogenic and proton-induced ^{21}Ne diffusivities in sample 04-RDY-139-STR also overlap at higher temperatures (Fig. 5B). A small fraction (7%) of the total ^{21}Ne in the cosmogenic experiment degassed at temperatures less than 250 °C; the diffusivities calculated for these steps plot above the proton-induced ^{21}Ne diffusivities at the same temperatures. In principle, if ^{21}Ne produced by proton irradiation is diffusively equivalent to cosmic-ray-produced Ne, we should observe exactly the same diffusion kinetics in natural and proton-irradiated samples. Although this is the case in broad terms, the results of the two experiments differ in detail. As discussed above, bulk Ne isotope ratios in this sample indicate that only 70% of the total ^{21}Ne is

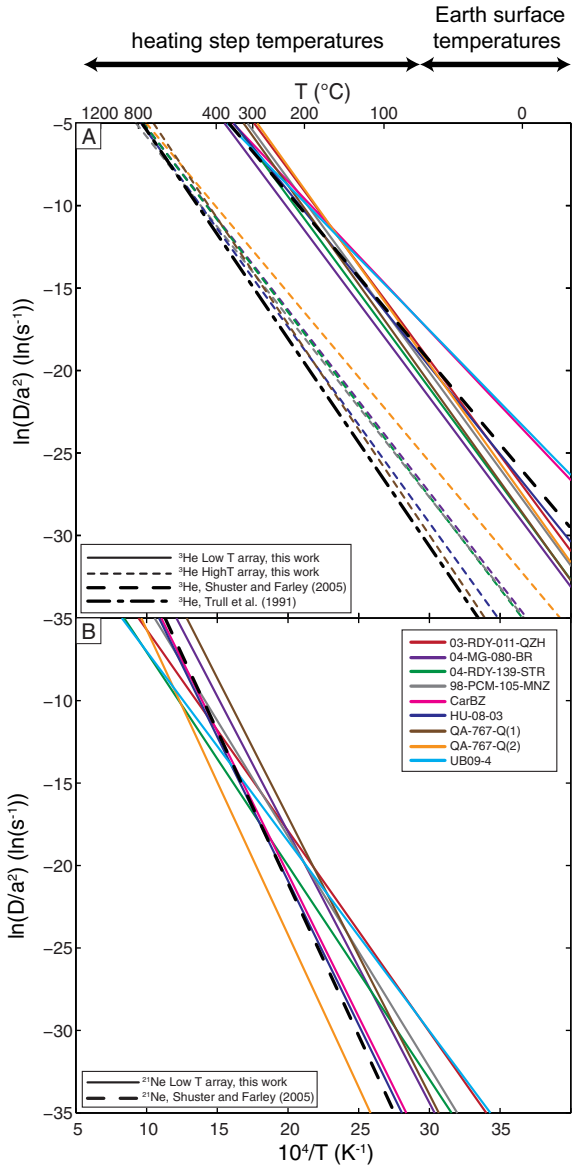

Fig. 4. Summary Arrhenius plot of the nine quartz diffusion experiments conducted in this study. In (A), solid colored lines correspond to the low-temperature linear arrays and dashed colored lines correspond to the high-temperature linear arrays observed for ^{3}He. In (B), the solid colored lines correspond to the low-temperature linear arrays observed for ^{21}Ne. Also plotted are the Arrhenius relationships for ^{3}He and ^{21}Ne diffusion in quartz reported by Shuster and Farley (2005) (dashed black) and for ^{3}He reported by Trull et al. (1991) (dashed-dotted black). Above the Arrhenius plot, the temperature range over which diffusion experiments occur and the temperature range characterizing the Earth's surface are shown. (For interpretation of the references to color in this figure legend, the reader is referred to the web version of this article.)

cosmic-ray-produced. Differences in the release pattern of cosmogenic and a "trapped" atmospheric ^{21}Ne component in this sample could therefore potentially explain differences between the two experiments. However, as noted above, amounts of Ne released in individual heating steps in the experiment on naturally irradiated quartz were too small to accurately separate ^{21}Ne released in each step into cosmogenic and "trapped" components.

We also observed two linear Arrhenius arrays in the step-degassing experiment on a proton-irradiated quartz fragment from sample HU-08-03, a rhyolite moraine boulder from Peru (Fig. 1). Bulk cosmogenic ^{3}He measurements for six aliquots of unirradiated quartz from this sample yield an average cosmogenic ^{3}He concentration of 3.75 ($\pm$0.3) Matoms/g; results from each analysis are reported in Table S4. We estimated the production rate of cosmogenic ^{3}He at this site by rescaling direct measurements of the ^{3}He production rate in synthetic quartz targets by Vermeesch et al. (2009). To do this, we used the scaling scheme of Stone (2000) as implemented in Balco et al. (2008), the elevation-atmospheric pressure relationship of Balco et al. (2008), and the solar variability calculations in Vermeesch et al. (2009). This yields an estimate of 1390 atoms/g/yr for the ^{3}He production rate at the site where HU-08-03 was collected. It is difficult to evaluate the accuracy of this estimate because of uncertainties in production rate scaling between high elevations at low and high latitudes (Lifton et al., 2014), so we assign a 10% uncertainty to this estimate based on the scaling uncertainty in ^{3}He production rate estimates estimated by Goehring et al. (2010). Given this production rate, the apparent exposure age of HU-08-03 from cosmogenic ^{3}He is 2700 $\pm$ 350 yr. The ratio of this apparent exposure age to the radiocarbon age of the moraine (12,350 + 200/−20 yr; Kelly et al., 2012, 2013) is 0.22 $\pm$ 0.03, which indicates that if the radiocarbon age represents the true exposure age of sample HU-08-03, ~75% of the cosmogenic ^{3}He produced during this sample's exposure history has been diffusively lost. Hereafter we refer to this ratio as ^{3}He retention (Tremblay et al., 2014).

3.3. Fluid and mineral inclusions

Examination of polished grain mounts provides us with a qualitative sense of the abundances and types of fluid and mineral inclusions characteristic of the quartz samples we studied in diffusion experiments. Example images from optical microscope and SEM analyses are provided in Fig. S9. Of the three quartz samples with one linear Arrhenius array observed in the step-degassing experiments, CarBZ and 03-RDY-011-QZH contain no visible fluid or mineral inclusions. Quartz fragments from sample 03-RDY-011-QZH are highly fractured, with cracks often penetrating deep into the interior of grains. We also only observed one linear Arrhenius array for sample UB09-4, yet SEM examination revealed that quartz from UB09-4 often contains inclusions of accessory minerals like apatite, zircon, and rutile. Some quartz fragments from UB09-4 also contain linear tracks of opaque fluid inclusions visible in plain light, although these are not abundant. Of the samples exhibiting two linear Arrhenius arrays in step-degassing experiments, the abundance and type of inclusions are highly variable. Quartz fragments from samples 04-MG-080-BR and 04-RDY-139-STR are dominated by abundant trails of

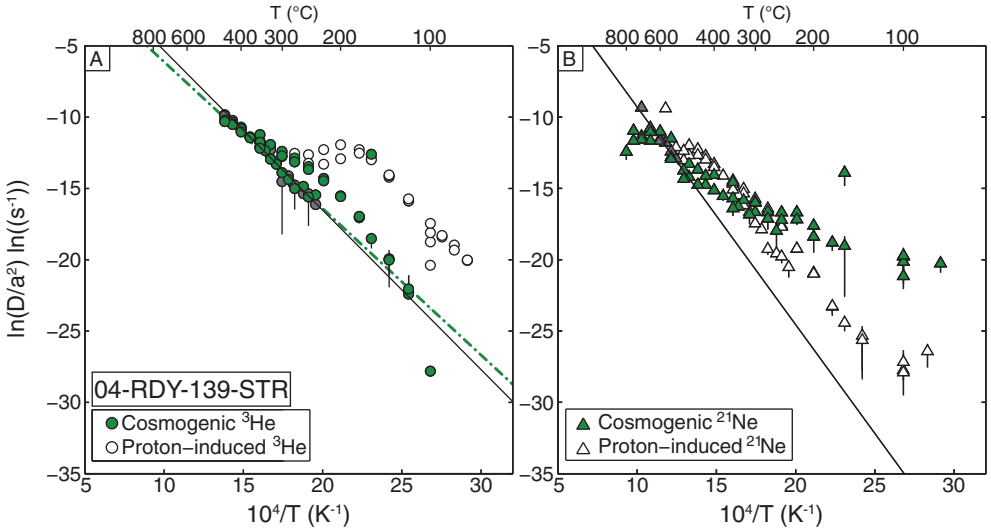

Fig. 5. Arrhenius plots for proton-induced and cosmogenic ^{3}He (A) and ^{21}Ne (B) diffusion for Antarctic vein quartz sample 04-RDY-139-STR. Unfilled and gray-filled symbols represent the $\ln(D/a^2)$ values for proton-induced ^{3}He and ^{21}Ne. Uncertainties are equivalent to those in Fig. S4. Here, we show with gray-filled symbols the heating steps that we used to calculate E_a and $\ln(D_0/a^2)$ for the higher-temperature linear Arrhenius arrays (Table 1). Linear regressions through these data are also shown. Green-filled symbols show the $\ln(D/a^2)$ values calculated for cosmogenic ^{3}He and ^{21}Ne. We propagated uncertainty in the cosmogenic $\ln(D/a^2)$ values using the same Monte Carlo approach that we used for the proton-irradiated experiments. The dashed-dotted green line in (A) shows the linear regression through the cosmogenic ^{3}He measurements corresponding to the same steps as the proton-induced ^{3}He measurements used to calculate E_a and $\ln(D_0/a^2)$ for the higher-temperature linear Arrhenius array. (For interpretation of the references to color in this figure legend, the reader is referred to the web version of this article.)

dark fluid inclusions. Fluid inclusions in these two samples make up a significant (although not quantified) volume of the quartz fragments. On the other hand, fluid inclusions are rare in quartz fragments from samples 98-PCM-105-MNZ, HU-08-03, and QA-767-Q, all of which exhibit two well-defined linear Arrhenius arrays in experiments. We found evidence for a fluid inclusion trail in one quartz fragment from sample HU-08-03 and occasional isolated fluid inclusions in other quartz fragments from these samples. We observed inclusions of the minerals zircon, apatite, and hornblende in quartz fragments from sample 98-PCM-105-MNZ, and numerous zircon inclusions were present in quartz from sample HU-08-03. We only found one inclusion of a feldspar in a quartz fragment of QA-767-Q.

3.4. Trace element concentrations

We report concentrations of Al, Ca, Fe, K, Li, Mg, Na, and Ti measured by ICP-OES for each of the quartz samples we conducted step-degassing experiments on in Table S5. Mn concentrations were below the detection limit in all samples and are therefore not reported. For five of the eight samples with sufficient material, we dissolved two separate aliquots of quartz; these replicates are listed in Table S5. Concentrations of all elements were below detection limit in two procedural blanks. All quartz samples contain measurable Al, with concentrations ranging from 15 to 650 ppm. Most quartz samples also contain measurable Li, Na, and Ti.

4. DISCUSSION

Numerous mechanisms could be responsible for the complex Arrhenius behavior observed in six of our nine experiments. As we discuss below, our results suggest that anisotropy and temperature-dependent structural transformations are unlikely causes. Instead, a sample-specific property, such as radiation damage, structural defects, mineral inclusions and fluid inclusions may be responsible for the complex Arrhenius behavior. While at present we cannot definitively explain this behavior, we present a simple two-domain model that, although lacking an underlying physical mechanism, closely reproduces the observed complex Arrhenius behavior. We then use this two-domain model framework and our measurements of cosmogenic ^{3}He and ^{21}Ne in sample HU-08-03 to test the applicability of our laboratory-determined diffusion kinetics at Earth surface temperatures and over geologic time.

4.1. Complex Arrhenius behavior

The low-temperature linear Arrhenius arrays observed in our experiments broadly agree with the single linear Arrhenius arrays observed for ^{3}He and ^{21}Ne diffusion in experiments reported by Shuster and Farley (2005) (Fig. 4). This indicates that these low-temperature arrays represent volume diffusion of ^{3}He and ^{21}Ne in our quartz samples. Below we explore potential mechanisms for producing complex Arrhenius behavior (i.e., the occurrence of, and transition between, low- and high-temperature

linear arrays) for ^{3}He and ^{21}Ne observed in some of our experiments.

Anisotropy is not the likely cause of the complex Arrhenius behavior for two reasons. First, we analyzed roughly equant quartz fragments in each diffusion experiment (i.e., the aspect ratios of the respective crystallographic axes were not extreme), but complex Arrhenius behavior was only observed in some of the experiments. We would expect each quartz fragment to exhibit two linear Arrhenius arrays if the arrays corresponded to diffusion along different crystallographic directions within the quartz lattice. Second, anisotropic diffusion occurs when the energy barriers associated with different diffusion pathways differ significantly enough such that one pathway is preferred at low temperatures and that multiple diffusion pathways are permitted at high enough temperatures (e.g., Reich et al., 2007). Thus there is a temperature dependence to which diffusion pathway is taken, and this temperature dependence should be expressed in both prograde and retrograde heating cycles. Yet in all cases where complex ^{3}He behavior is observed, the diffusivities defining the second linear array correspond to both prograde and retrograde heating steps to below the transition (e.g., Figs. 1A and 2A) and do not agree with the diffusivities in the preceding transition zone. Collectively, these lines of evidence are inconsistent with the hypothesis that multiple Arrhenius arrays are the result of anisotropic diffusion.

The observed temperatures of the apparent transition in D/a^2 also make structural transformations in quartz an unlikely cause of complex Arrhenius behavior. The only structural transformation expected to occur in quartz during the main phase of our experiments (i.e., not the final highest temperature steps) is the α-quartz to β-quartz transformation. The α- to β-quartz transformation occurs instantaneously at ~573 °C at 1 atm (Heaney and Veblen, 1991, and references therein) and likely occurs at a similar temperature in our experiments under vacuum. At temperatures preceding the α- to β-quartz transformation, α-quartz experiences systematic volume expansion; after the transition, β-quartz experiences no volume expansion at temperatures below 1000 °C (Ackermann and Sorrell, 1974). We thus expect a change in diffusive behavior of ^{3}He and ^{21}Ne across the α- to β-quartz transformation. Yet the transition between the initial low-temperature linear array and the subsequent high-temperature array occurs at temperatures ⩽450 °C for ^{3}He in all experiments where we observed the transition. The α-quartz to β-quartz transformation likely does affect the diffusive behavior of ^{21}Ne in our experiments, since deviation from the first linear Arrhenius array generally occurs between 400 and 600 °C. Further, the Pt–Ir packets are allowed to cool during analyses in between heating steps, which means that quartz fragments undergo the instantaneous α- to β-quartz transformation multiple times towards the end of the diffusion experiments. Repeated transformation between α-quartz to β-quartz may explain why second high-temperature ^{21}Ne arrays consistent with ^{3}He high-temperature arrays are not always observed. This may also explain why activation energies for high-temperature ^{21}Ne arrays are inconsistent with activation energies of the low-temperature ^{21}Ne arrays, in cases where high-temperature ^{21}Ne and ^{3}He agreement is observed. Ultimately, these inconsistencies in ^{21}Ne behavior at or above the α- to β-quartz transformation temperature indicate that only the low-temperature linear array for ^{21}Ne observed in our experiments should be extrapolated to Earth surface temperatures. In future experiments, degassing most of the ^{21}Ne through longer heating steps at temperatures below the α- to β-quartz transformation temperature may result in a better resolved second linear Arrhenius array for ^{21}Ne.

The fact that in most experiments we observed departures from the low-temperature Arrhenius arrays at nearly equivalent cumulative release fractions of ^{3}He and ^{21}Ne (Figs. 1C and 2C) but different temperatures for each nuclide (Figs. 1B and 2B) is significant for several reasons. In addition to the arguments above about anisotropy and the α- to β-quartz transformation, this observation indicates that the ^{3}He diffusivity transition is not due to a material property change. Otherwise, diffusivities of both nuclides would be expected to deviate from linear Arrhenius behavior at a common temperature. Further, the relationship between low-temperature Arrhenius arrays and cumulative release fractions suggests that the patterns of ^{3}He and ^{21}Ne diffusive behavior are controlled by a common mechanism at temperatures <573 °C. Since this behavior is not observed in all experiments, and the cumulative gas fraction comprising the first linear arrays varies between experiments, this behavior must be controlled by a sample-specific property such as radiation damage, mineral inclusions, fluid inclusions, or structural defects. We discuss each of these sample-specific properties and its potential link with diffusive behavior below.

The diffusion kinetics of noble gases in quartz may be influenced by natural radiation damage, due to U and Th present either in the quartz itself or in surrounding or included accessory minerals, or by damage associated with proton irradiation. With regards to the latter, Shuster and Farley (2005) calculated slightly different ^{3}He and ^{21}Ne diffusion parameters in experiments on two fragments of the same quartz sample irradiated with different proton energies and fluences; the fragment experiencing the higher proton dose exhibits slightly greater ^{3}He and ^{21}Ne retentivity. We did not irradiate individual samples with different proton doses and therefore cannot evaluate whether the proton irradiation influenced the diffusion kinetics inferred from linear Arrhenius arrays. However, the results of our stepwise degassing experiment on non-irradiated quartz fragments from sample 04-RDY-139-STR clearly demonstrate that complex Arrhenius behavior is not an artifact of the proton irradiation. For cosmogenic ^{3}He, we observed significantly lower apparent diffusivities at temperatures corresponding to the low temperature linear Arrhenius array in the proton-irradiated experiment, consistent with diffusive loss over this sample's exposure history at subzero temperatures in Antarctica. In contrast, we find excellent agreement between apparent diffusivities of cosmogenic and proton-induced ^{3}He corresponding to the high temperature linear Arrhenius array (Fig. 5A). This has two important implications. First, that the high-temperature array in proton-irradiated quartz is also present in the diffusive

behavior of non-irradiated quartz indicates that this behavior not an artifact of the irradiation. Second, given likely mean annual temperatures at this elevation in the southern Transantarctic Mountains near −40 °C, we expect significant diffusive loss of ^{3}He based on the low-temperature Arrhenius array, but insignificant (<5%) loss based on the high-temperature Arrhenius array. This observation may indicate that ^{3}He, and by inference ^{21}Ne, are hosted in two separate reservoirs in quartz characterized by the diffusion parameters calculated for each linear Arrhenius array. We explore this possibility in a two-domain model constructed in Section 4.2.

At relatively low doses, the accumulation of natural radiation damage is known to increase He retentivity in minerals like apatite (Shuster and Farley, 2009; Shuster et al., 2006; Flowers et al., 2009) and zircon (Guenthner et al., 2013), and cathodoluminescence and electron paramagnetic resonance (EPR) analyses demonstrate that α-particles produced by U and Th decay induce structural defects in quartz, in particular silicon vacancies and peroxy linkages (Botis et al., 2005; Krickl et al., 2008). If damage induced by natural radiation influences noble gas diffusion in quartz, as it does in apatite and zircon, we expect this damage to have similar effects on cosmogenic and proton-induced noble gas diffusion in quartz. This is because natural radiation damage, unlike damage produced during proton irradiation, will accumulate in quartz on geologic timescales, presumably starting long before quartz samples are exposed to cosmic rays at the Earth's surface. That the quartz fragments we analyzed come from geologic samples with vastly different ages, from Precambrian metamorphic rocks to Miocene volcanics, indicates that these samples likely have very different amounts of natural radiation damage. To assess this more directly, we calculated the amount of ^{4}He present in each sample prior to proton irradiation (Table S6) by simply subtracting the proton-induced ^{4}He from the total observed ^{4}He and assuming a production ^{4}He/^{3}He ratio of ~8.5 and that all observed ^{3}He is proton-induced (e.g., Shuster and Farley, 2005). Assuming that most of the inherent ^{4}He is radiogenic and therefore a proxy for the amount of radiation damage accumulated, we find no correlation between complex Arrhenius behavior and radiation damage, nor do we find an obvious relationship between the diffusion parameters for the first linear Arrhenius array and radiation damage. Additionally, the concentrations of ^{4}He in the two quartz fragments from sample QA-767-Q vary by a factor of seven, but the results of the two diffusion experiments are remarkably consistent. We realize, however, that the concentration of ^{4}He in our quartz samples is a non-ideal proxy for radiation damage, since ^{4}He experiences diffusive loss from quartz at Earth surface temperatures and because non-radiogenic ^{4}He may also be present in these samples. In the future, measuring U and Th concentrations in quartz samples analyzed in diffusion experiments should provide a more robust measure of the effects of radiation damage on noble gas diffusion kinetics.

In addition to radiation-induced damage, numerous point defects, dislocations or line defects, and twinning boundaries have been commonly identified in naturally occurring quartz (e.g., Götze, 2009) that may influence noble gas diffusive behavior. We observed no systematic correlation between the concentrations of any trace element commonly associated with point defects and the observation of one or two linear Arrhenius arrays in step-degassing experiments (Table S5). Likewise, we observed no systematic correlation between trace element concentration and the fraction of ^{3}He and ^{21}Ne represented by the low-temperature linear Arrhenius arrays when two arrays were observed. While these observations indicate that point defects commonly associated with trace elements in quartz do not likely contribute to the observed complexity in noble gas diffusion, there are a number of point defects in quartz not associated with trace elements that we have not attempted to identify or evaluate here, including peroxy linkages, oxygen vacancies, silicon vacancies, and non-bridging oxygen holes. Additionally, we have not attempted to quantify the density of line or plane defects in our quartz samples. A series of inward diffusion experiments provide evidence for "fast-path" diffusion of noble gases in quartz, either by edge/screw dislocations (Argunova et al., 2003; Clay et al., 2010) or via isolated "nanopores" ranging in size from 10 to 70 nm (Watson and Cherniak, 2003). When considered in the context of our step-degassing experiments, these experimental results point to the possibility that line and plane defects that do not intersect the boundaries of a quartz grain act as noble gas sinks, similar to how radiation damage in apatite creates pockets or "traps" where He can accumulate (Shuster et al., 2006; Flowers et al., 2009). Thus structural defects in quartz remain a strong potential candidate for explaining the complex diffusive behavior of ^{3}He and ^{21}Ne observed in our experiments.

Fluid and mineral inclusions in the quartz samples we analyzed are highly variable and do not correlate systematically with complex Arrhenius behavior. Many of the quartz samples displaying such complexity contain accessory minerals like zircon and apatite. When present, accessory mineral inclusions are smaller than 20 μm in diameter and do not make up a significant volume of the quartz fragments, which are generally 200 μm in diameter or larger (Fig. S9). Because spallogenic ^{3}He and ^{21}Ne are produced in these accessory mineral inclusions during proton irradiation at rates similar to production rates in the quartz matrix (e.g., Shuster et al., 2004), they constitute an insignificant fraction of the total ^{3}He and ^{21}Ne abundances and therefore cannot account for the volume of gas associated with the higher-temperature array sometimes observed. Further, apatite, zircon, and rutile inclusions are common in quartz fragments from sample UB09-4, for which we observed only one linear Arrhenius array.

Visible fluid inclusions 5–15 μm in diameter occurred in the quartz analyzed by Trull et al. (1991). The ^{3}He diffusion parameters those authors calculated agree well with the ^{3}He diffusion parameters we calculated for the high-temperature linear Arrhenius arrays, indicating that fluid inclusions may be responsible for complex Arrhenius behavior. We found evidence for fluid inclusions in at least one quartz fragment for all of the samples that exhibited complex Arrhenius behavior. However, the abundance of fluid inclusions varies significantly amongst these quartz

samples. While fluid inclusion trails make up a significant volume of the quartz fragments in two of the samples (Fig. S9B, C), fluid inclusions are rare and isolated in other quartz samples exhibiting complex Arrhenius behavior (Fig. S9D, F, G, H). Given that fluid inclusions in our quartz samples are almost always smaller than 10 μm, it seems unlikely that sufficient abundances of ^{3}He and ^{21}Ne were produced in fluid inclusions to constitute the higher temperature linear Arrhenius arrays observed in the samples with rare fluid inclusions. Additionally, we observed no correlation between complex Arrhenius behavior and concentrations of Ca, K, Mg, or Na, elements that are often concentrated in fluid inclusions (e.g., Götze et al., 2004). An important caveat is that the composition of the fluid inclusions dictates the partition coefficient of ^{3}He and ^{21}Ne between the fluid inclusions and quartz, and the specific compositions of the fluid inclusions in the quartz samples we analyzed are unknown. Thus fluid inclusions remain a viable potential contributor to the complex Arrhenius behavior observed in some experiments.

4.2. Comparison with results of Shuster and Farley (2005)

Shuster and Farley (2005) conducted step-degassing experiments on gem-quality quartz from Brazil that exhibited single linear Arrhenius arrays for both ^{3}He and ^{21}Ne. Shuster and Farley (2005) did not measure all of the ^{21}Ne present in their irradiated quartz aliquots in the step-degassing portion of their experiments (~40% and 10% of the gas was extracted in the final fusion step of the high-dose and low dose experiment, respectively). Additionally, there is a slight deviation from the linear Arrhenius array for ^{21}Ne at the end of their low-dose experiment similar to the transition zone observed in our experiments. From these two observations one can speculate that Shuster and Farley (2005) may have observed complex diffusion behavior of ^{21}Ne if they had continued measuring ^{21}Ne in the step-heating portion of their experiment. However, Shuster and Farley (2005) completely degassed helium during the step-heating portion of their experiments and did not observe any deviation from a linear array. Therefore we do not think that this methodological difference is responsible for the differences between their results and the results presented here.

The Arrhenius parameters calculated from a different Brazilian gem-quality quartz sample analyzed here (sample CarBZ) indicate much greater ^{3}He and ^{21}Ne diffusivity than the sample analyzed in Shuster and Farley (2005). In addition, the final ~40% of gas released in the experiment on CarBZ deviates from the linear Arrhenius array. The differences in diffusion kinetics and behavior between these two gem-quality samples, both of which lack fluid and mineral inclusions, supports the hypothesis that these differences are caused by inter-sample variability in material properties—specifically radiation damage and/or structural defects—that are not quantitatively measured here. Unfortunately, we do not have sufficient material from the sample analyzed in Shuster and Farley (2005) to test this hypothesis directly.

4.3. Two-domain model for ^{3}He diffusion in quartz

Although we have not identified a mechanistic explanation for the complex diffusive behavior of proton-induced ^{3}He and ^{21}Ne in quartz, our step-degassing experiment on the naturally irradiated aliquot of quartz sample 04-RDY-139-STR clearly demonstrates that the mechanism driving complex behavior influences cosmogenic noble gas retention over geologic time. Deviations from simple Arrhenius linearity similar to those observed in our experiments are often observed for Ar in feldspars. This led to the development of multiple diffusion domain (MDD) theory, whereby the non-linearity is explained by the systematic exhaustion of sub-grain domains with unique diffusion kinetics (e.g., Lovera et al., 1989, 1997). Lacking a mechanistic model, we took a similar approach and used the sample-specific diffusion parameters for the low and high temperature linear Arrhenius arrays to construct a simple two-domain diffusion model for noble gas diffusion in each quartz sample exhibiting two linear arrays. Like MDD models, these empirical models assume that the quartz fragments analyzed contain two, non-interacting domains that each make up a fraction of the total quartz fragment volume in which ^{3}He and ^{21}Ne can reside. Domain 1 refers to the lower retentivity domain characterized by the diffusion parameters of the low-temperature linear Arrhenius array from each diffusion experiment; domain 2 refers to the high retentivity domain characterized by the diffusion parameters of the higher-temperature linear Arrhenius arrays when observed. The fact that we observe divergence from the low-temperature Arrhenius array at the same cumulative gas release fraction for both He and Ne implies that the same two-domain model is appropriate for both noble gases. However, as discussed above, we are less likely to have accurately quantified the diffusion kinetics of the higher-temperature domain for Ne, so we only construct these models using the ^{3}He diffusion kinetics from our experiments. Because the ^{21}Ne diffusion kinetics for the low-temperature domain imply complete retention at Earth surface temperatures in most quartz samples, these models are less relevant to the interpretation of ^{21}Ne abundances in natural samples (see Section 4.4 below).

In the two-domain model, the proportion of ^{3}He in each domain is allowed to vary, and diffusivities are calculated for the same heating schedule as used in the proton-irradiated experiment using the equations outlined by Fechtig and Kalbitzer (1966). We determined the proportion of ^{3}He in each domain that best agreed with the experimental data by calculating a misfit statistic M:

$$M = \frac{1}{n}\sum_{j=1}^{n}\left(\frac{f_{p,j} - f_{m,j}}{\bar{\sigma}}\right)^{2} \quad (1)$$

where $f_{p,j}$ is the modeled cumulative release fraction of ^{3}He at heating step j, $f_{m,j}$ is the cumulative release fraction of ^{3}He measured during heating step j in the experiment, $\bar{\sigma}$ is the mean uncertainty in the cumulative release fractions of ^{3}He determined from the Monte Carlo simulation, and n is the number of steps in each heating schedule. Modeled diffusivities for ^{3}He using the domain proportions that

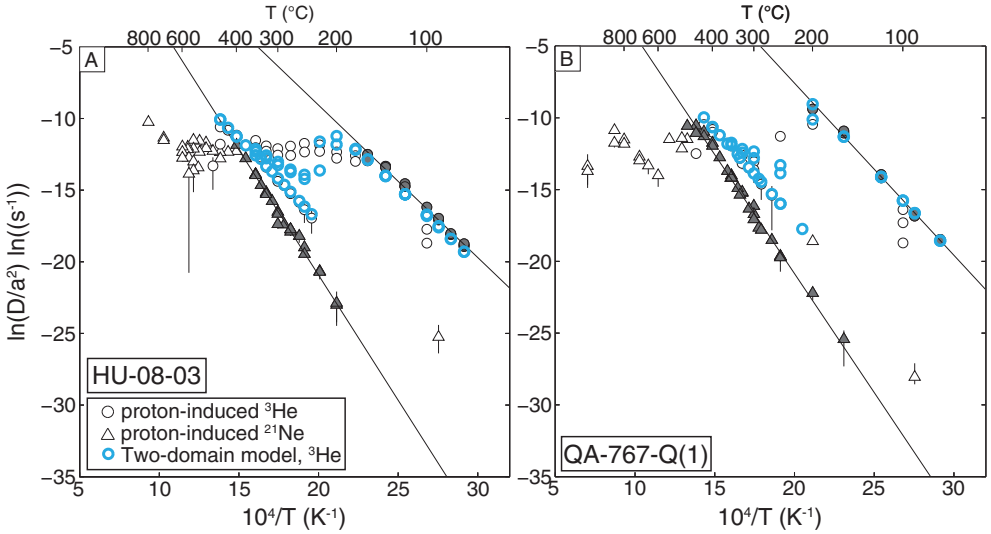

Fig. 6. Arrhenius plots of the two-domain models for ^{3}He diffusion in quartz samples HU-08-03 (A) and QA-767-Q(1) (B). The results of the diffusion experiment on proton-irradiated quartz fragments corresponding to Figs. 1A and 2A are shown for comparison with the two-domain model (blue circles). The proportion of gas apportioned to the two domains minimized the misfit statistic M discussed in Section 4.3. For HU-08-03 (A), the two-domain model predicts that 81% of the ^{3}He is resides in domain 1, with the remaining 19% populates domain 2. For QA-767-Q(1) (B), only 1% of the ^{3}He is expected to be hosted in domain 2. (For interpretation of the references to color in this figure legend, the reader is referred to the web version of this article.)

minimized this misfit statistic are shown in Arrhenius space for samples HU-08-03 and QA-767-Q(1) in Fig. 6 and in Fig. S10 for the other four experiments exhibiting two linear Arrhenius arrays. The two-domain models reproduce the two linear Arrhenius arrays observed in experiments as expected, but generally differ from the steps in the experiment corresponding to the transition zone. The amount of gas apportioned to domain 1 ranges from 75% to 99% (Table S7), which in each of the diffusion experiments corresponds well with the low-temperature linear Arrhenius array and a portion of the transition zone. For the remaining discussion we continue to use the two-domain model framework, recognizing that a model with stronger mechanistic underpinnings is important for future work.

4.4. Implications for He and Ne retentivity in quartz

The nine diffusion experiments we conducted on a variety of quartz samples demonstrate that both the diffusion kinetics and diffusive behavior of ^{3}He and ^{21}Ne in quartz are quite variable. This implies that retentivity of cosmogenic ^{3}He and ^{21}Ne at Earth surface temperatures can vary significantly as well. Fig. 7 shows expected variation in cosmogenic ^{3}He and ^{21}Ne retentivity during an example continuous exposure history given the ^{3}He and ^{21}Ne diffusion parameters calculated from each diffusion experiment. To highlight the effect of apparent MDD-like behavior of ^{3}He observed in some experiments on cosmogenic ^{3}He retention during surface exposure, we show separate retentivity curves for He diffusion parameters inferred from the two separate linear Arrhenius arrays (Fig. 7A). He diffusion parameters calculated for the low-temperature linear Arrhenius arrays imply that all quartz samples analyzed will experience significant diffusive loss of cosmogenic ^{3}He even at subzero surface temperatures, which is consistent with the conclusions of Shuster and Farley (2005). However, the diffusion parameters of the high-temperature linear Arrhenius arrays indicate nearly complete retention of ^{3}He in the postulated high-retentivity domain at temperatures near or well above 0 °C in large quartz grains. This contrast is important for potential applications of cosmogenic ^{3}He in quartz to exposure-dating and paleothermometry (Tremblay et al., 2014), as a two-domain model predicts partial retention of cosmogenic ^{3}He over a wider range of temperatures and exposure times than either domain by itself.

The variability we observed in ^{21}Ne diffusion kinetics among samples is less important from the perspective of cosmogenic ^{21}Ne retention at Earth surface temperatures, because in nearly all cases the experimental results predict that >95% of cosmogenic ^{21}Ne produced in quartz will be retained at temperatures <40 °C for diffusion domain radii >500 μm (Fig. 7B). ^{21}Ne retentivities are shown using only the diffusion parameters of the low-temperature linear Arrhenius arrays; diffusion parameters for the high-temperature array in three experiments imply even greater retention. Given that temperatures consistently exceeding 40 °C occur in very few places on Earth, our experiments indicate that cosmogenic ^{21}Ne will generally be quantitatively retained in quartz over geologic time. This is consistent with the results of Shuster and Farley (2005) and numerous measurements of cosmogenic ^{21}Ne exposure ages in quartz that agree with exposure ages determined using other cosmogenic radionuclides (e.g., Hetzel et al., 2002; Kober et al., 2007; Balco and Shuster, 2009). In the most qualitative sense, this interpretation is also consistent with the Ne diffusion kinetics estimated from the inward diffusion experiments conducted by Cherniak et al. (2014); however, they

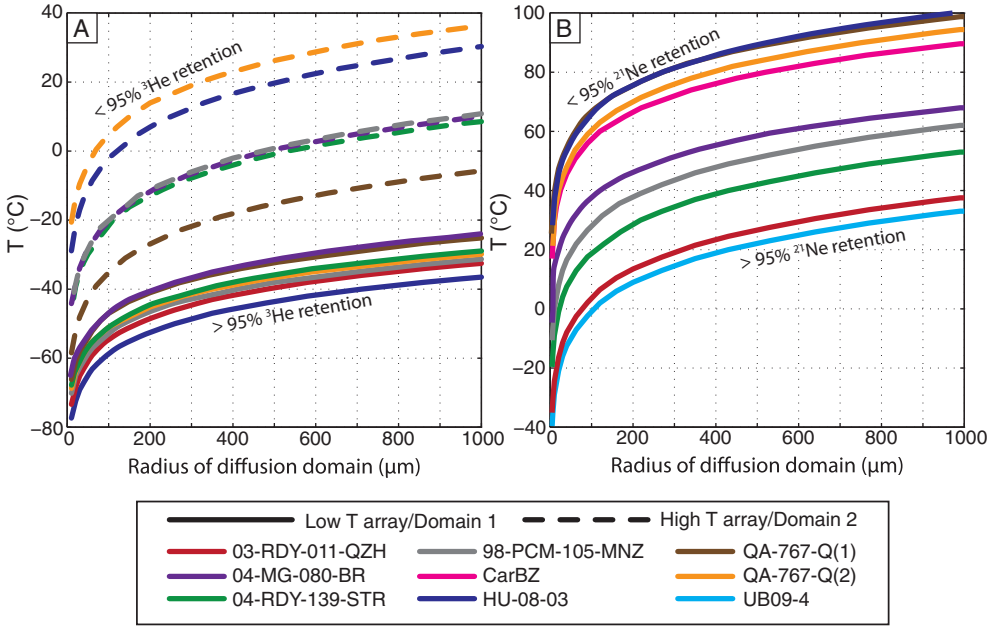

Fig. 7. Helium (A) and neon (B) retentivity in quartz. The curves show threshold temperatures above which <95% retention would occur in quartz as a function of diffusive length scale for isothermal simultaneous production and diffusion over 50,000 years, calculated after Wolf et al. (1998). For ^{3}He (A), the threshold temperature–diffusive length scale relationship is shown for the diffusion kinetics calculated for both the low temperature (solid) and high temperature (dashed) linear Arrhenius arrays when observed in diffusion experiments. Retentivity curves for ^{3}He in quartz samples UB09-4 and CarBZ plot below the temperature range shown. For ^{21}Ne (B), retentivity curves are only shown for the first linear Arrhenius array observed in diffusion experiments.

calculated diffusion parameters that predict Ne diffusivities six orders of magnitude lower than the most retentive quartz sample we analyzed. As mentioned previously, the very small length scales over which inward diffusion experiments like those of Cherniak et al. (2014) are conducted avoid the physical heterogeneities in quartz that—as our experiments demonstrate—can significantly influence the net, grain-scale diffusion of noble gases from natural quartz that we are ultimately interested in quantifying.

Importantly, and in contrast to the experiments of Cherniak et al. (2014), some of the experiments we conducted imply that quantitative retention of cosmogenic ^{21}Ne does not always occur at moderately high surface temperatures. For example, the experiments on quartz samples 03-RDY-011-QZH and UB09-4 predict that, at temperatures of 20–40 °C, detectable diffusive loss of cosmogenic ^{21}Ne will occur over short exposure times and significant diffusive loss will occur after 10^{6}–10^{7} yr of exposure. The activation energy estimated by Niedermann et al. (1993) for ^{21}Ne diffusion in quartz of 90 ± 10 kJ/mol agrees with those calculated from the experiments on 03-RDY-011-QZH and UB09-4 within uncertainty and predicts similar diffusive behavior at relatively high surface temperatures. This variability in ^{21}Ne diffusion kinetics is potentially important in interpreting old apparent exposure ages inferred from cosmogenic ^{21}Ne concentrations in quartz in hot environments (e.g., Dunai et al., 2005).

The variability in ^{3}He and ^{21}Ne retentivity inferred from our diffusion experiments and from previous estimates of ^{3}He and ^{21}Ne diffusivities in quartz from step-degassing measurements (Trull et al., 1991; Niedermann et al., 1993; Shuster and Farley, 2005) indicates that sample-specific diffusion parameters are required to quantitatively apply the open-system behavior of these nuclides to geologic problems. Our results predict that quartz grains in rocks sharing a common exposure duration and temperature but characterized by different diffusion kinetics can contain significantly different abundances of cosmogenic noble gases. Thus if we measure the abundances of cosmogenic noble gases in quartz from a geologic sample, we may come to drastically different inferences about the exposure duration and/or temperature of that sample depending on the set of diffusion kinetics we assume. We illustrate this point below with measurements of cosmogenic ^{3}He in sample HU-08-03.

4.5. Geologic applicability of laboratory-determined diffusion kinetics

To test whether our laboratory-determined diffusion kinetics for ^{3}He accurately quantify cosmogenic ^{3}He diffusion under natural conditions, we compare the retention of cosmogenic ^{3}He we observed in quartz sample HU-08-03, a rhyolitic moraine boulder adjacent to the Quelccaya ice cap in Peru, with the retention predicted from our step-degassing experiments. The data point in Fig. 8A and B indicates the observed cosmogenic ^{3}He retention of 0.22 ± 0.03 calculated in Section 3.2. In Fig. 8A, we predict cosmogenic ^{3}He retention as a function of time and a constant effective diffusion temperature (EDT; Tremblay et al., 2014) using the laboratory-determined diffusion parameters for HU-08-03, the average grain size of the quartz analyzed for cosmogenic ^{3}He ($a = 300$ μm), and two models. In one

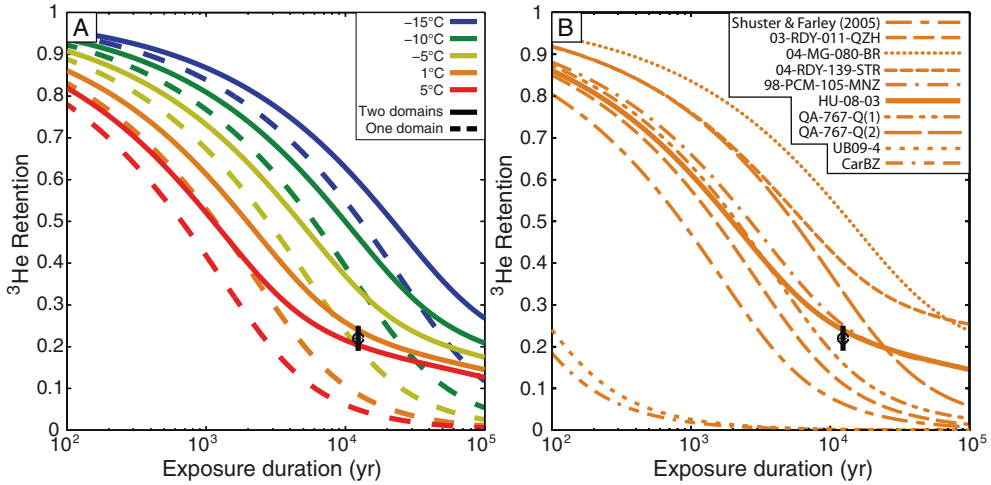

Fig. 8. Retention of cosmogenic ^{3}He in sample HU-08-03, calculated from ^{3}He measurements on six quartz aliquots. The known radiocarbon age for the moraine on which this sample was collected is 12,350 + 200/−20 yr (Kelly et al., 2012, 2013). In (A), the observed cosmogenic ^{3}He retention is compared to the predicted evolution of ^{3}He retention using the laboratory-determined diffusion parameters for HU-08-03 for different isothermal holding temperatures, calculated after Wolf et al. (1998). ^{3}He retention evolution curves are calculated using the diffusion parameters for only the low-temperature linear Arrhenius array (dotted) and the diffusion parameters for both linear Arrhenius arrays using the two-domain model (solid). In (B), the observed cosmogenic ^{3}He retention is compared to the predicted evolution of ^{3}He retention using the laboratory-determined diffusion parameters from all experiments for an isothermal holding temperature of 1 °C, the effective diffusion temperature (EDT) at the moraine today. For experiments in which complex Arrhenius behavior was observed, the two-domain model is shown. The ^{3}He retention curve for the diffusion parameters reported by Shuster and Farley (2005) is also shown.

model, we only use He diffusion kinetics represented by the low-temperature linear Arrhenius array. In the other model, we assume ^{3}He occupies two domains and use the diffusion kinetics and relative domain proportions from fitting a two-domain model (Table S7) to the experimental data (Fig. 6A).

For the one-domain model, the measured cosmogenic ^{3}He retention is consistent with an EDT of −5.8 (+1.2/−1.0)°C if only the uncertainty in cosmogenic ^{3}He retention is considered (this includes uncertainty in both the observed ^{3}He concentration and 10% uncertainty in the production rate). However, if uncertainties in both the cosmogenic ^{3}He retention and the diffusion kinetics for the one-domain model are considered, EDTs between −3.4 and −8.2 °C are consistent with the observed cosmogenic ^{3}He retention. For the two-domain model, the measured cosmogenic ^{3}He retention is consistent with an EDT of 3.0 (+4.1/−2.9)°C if solely uncertainty in the cosmogenic ^{3}He retention is included, and between −0.4 and 9 °C if uncertainties in both the cosmogenic ^{3}He measurements and the diffusion kinetics for the two-domain model are propagated.

In order to quantify daily and annual fluctuations in local temperature and calculate the EDT this sample actually experienced during exposure, we obtained hourly and monthly air temperature measurements from a USCRN-compatible weather station at Quelccaya ice cap for the period 2007–2013 from Doug Hardy of the University of Massachusetts Amherst and corrected temperatures for the elevation difference between the weather station and moraine using a local lapse rate determined from NCEP reanalysis data (Bradley et al., 2009). The calculation of an EDT accounts for the fact that diffusivity is a nonlinear function of temperature and that therefore the effective temperature—corresponding to the mean diffusivity experienced by the quartz sample over these short-term temperature oscillations—is higher than the mean temperature (Tremblay et al., 2014). Because of the daily and annual temperature amplitudes at this low-latitude site, the EDT we calculate of 1 °C is very close to the mean annual temperature (MAT) of ~0.1 °C. This also means that the EDT calculated using the diffusion parameters for the low and high-temperature linear Arrhenius arrays observed in the diffusion experiment on HU-08-03 are indistinguishable.

Fig. 8A shows that if we assume an EDT of 1 °C applies for the entire exposure history of this sample, we find that the one domain approach predicts significantly lower ^{3}He retention than observed. In other words, the EDT expected from the cosmogenic ^{3}He measurements and one-domain model (between −3.4 and −8.2 °C) is significantly different from the EDT expected from the modern climatology. The two-domain model, on the other hand, predicts ^{3}He retention indistinguishable from the observed retention for EDTs (between −0.4 and 9 °C) consistent with the modern climatology. We suggest that the EDT based on the modern climatology is a minimum estimate for the EDT this sample experienced during exposure, since we have not accounted for the effect of radiative heating of the sample surface on daily temperature amplitudes, nor have we accounted for evidence that temperatures at Quelccaya ice cap were warmer during the mid-Holocene (Thompson et al., 1995). Nonetheless, this result provides two important insights about the geologic applicability of our diffusion experiments and two-domain models. First, it demonstrates that solely considering the diffusion parameters for the

low-temperature linear Arrhenius arrays in our experiments does not adequately quantify the diffusive behavior of cosmogenic ^{3}He at the grain scale. Second, it indicates that although not framed by a physical mechanism, the two-domain model based on laboratory diffusion kinetics accurately predicts the diffusive loss of cosmogenic ^{3}He in a geologic setting.

In Fig. 8B, we use the same approach for modeling retention to highlight the importance of sample-specific diffusion kinetics for quantitative prediction of cosmogenic ^{3}He retention in geologic settings. We calculate ^{3}He retention using diffusion parameters from each of our nine diffusion experiments as well as that of Shuster and Farley (2005). As with the comparison in Fig. 8A, the EDT is not sensitive to the diffusion parameters used in its calculation at this location; therefore we model ^{3}He retention for an EDT of 1 °C using each set of diffusion parameters. In experiments where we observed two linear Arrhenius arrays, we used the two-domain model fit to the experimental results. For the known exposure age of ~12.4 ka, we find that most calculated retention curves, including that implied by Shuster and Farley (2005), disagree with measured cosmogenic ^{3}He retention. This result, in combination with the results shown in Fig. 8A, demonstrates the importance of obtaining sample-specific diffusion kinetics for geologic applications. Further, this result confirms that simply applying the ^{3}He diffusion parameters reported by Shuster and Farley (2005) to quartz is in this case inappropriate.

5. CONCLUSIONS

A series of nine diffusion experiments on proton-induced ^{3}He and ^{21}Ne in quartz reveal that ^{3}He and ^{21}Ne exhibit variable and complex diffusive behavior in different natural quartz samples. We hypothesize that sample-specific features such as radiation damage, defects, or inclusions control the diffusive behavior we observed, although we were not able to identify a clear correlation between diffusion kinetics and any easily observable physical property of the samples. Measurements of cosmogenic ^{3}He and ^{21}Ne in some of the same samples demonstrate that complex diffusive behavior observed for proton-induced ^{3}He and ^{21}Ne is not an artifact of producing these nuclides via proton irradiation and needs to be accounted for in geologic applications. Identifying what controls complex and variable diffusive behavior of noble gases in quartz and developing mechanism-based diffusion models is thus an important direction for future research. To a first order, the ^{3}He and ^{21}Ne diffusion kinetics we observed in quartz are consistent with previous experiments and empirical observations suggesting that cosmogenic ^{3}He will experience significant diffusive loss from quartz on timescales $>10^3$ yr even at subzero temperatures, while cosmogenic ^{21}Ne will be quantitatively retained at nearly all Earth surface temperatures for $>10^6$ yr. Importantly, the results presented here facilitate quantitative applications of these phenomena in determining both paleotemperatures and exposure durations from cosmogenic ^{3}He and ^{21}Ne concentrations.

ACKNOWLEDGEMENTS

We thank B. Goehring and J. Schafer for providing information about and material from sample UB09-4, D. Rood for providing material from sample QA-767-Q, J. Stone for providing material and exposure-age data from samples 04-RDY-139-STR and 98-PCM-105-MNZ, and R. Wenk for providing sample CarBZ. We thank P. Brooks, N. Fylstra, T. Becker, and T. Teague for analytical assistance, and D. Hardy for sharing data from the Quelccaya ice cap weather station. S. Cox and an anonymous reviewer provided thorough and thought provoking comments that helped strengthen this work. We acknowledge support from the NSF Petrology and Geochemistry Program (EAR-1322086), the UC Berkeley Larsen Grant, and the Ann and Gordon Getty Foundation.

APPENDIX A. SUPPLEMENTARY DATA

Supplementary data associated with this article can be found, in the online version, at http://dx.doi.org/10.1016/j.gca.2014.08.010.

REFERENCES

Ackermann R. J. and Sorrell C. A. (1974) Thermal expansion and the high-low transformation in quartz. I. High-temperature X-ray studies. *J. Appl. Crystallogr.* **7**, 461–467.

Ackert, Jr., R. P., Mukhopadhyay S., Pollard D., DeConto R. M., Putnam A. E. and Borns, Jr., H. W. (2011) West Antarctic Ice Sheet elevations in the Ohio range: geologic constraints and ice sheet modeling prior to the last highstand. *Earth Planet. Sci. Lett.* **307**, 83–93.

Argunova T. S., Sorokin L. M., Pevzner B. Z. and Balitski V. S. (2003) The influence of defects in the crystal structure on helium diffusion in quartz. *Phys. Solid State* **45**, 1910–1917.

Balco G. and Shuster D. L. (2009) Production rate of cosmogenic ^{21}Ne in quartz estimated from ^{10}Be, ^{26}Al, and ^{21}Ne concentrations in slowly eroding Antarctic bedrock surfaces. *Earth Planet. Sci. Lett.* **281**, 48–58.

Balco G., Stone J. O., Lifton N. A. and Dunai T. J. (2008) A complete and easily accessible means of calculating surface exposure ages or erosion rates from ^{10}Be and ^{26}Al measurements. *Quat. Geochronol.* **3**, 174–195.

Baxter E. F. (2010) Diffusion of noble gases in minerals. *Rev. Mineral. Geochem.* **72**, 509–557.

Botis S., Nokhrin S. M., Pan Y., Xu Y., Bonli T. and Sopuck V. (2005) Natural radiation-induced damage in quartz. I. Correlations between cathodoluminence colors and paramagnetic defects. *Can. Mineral.* **43**, 1565–1580.

Bradley R. S., Keimig F. T., Diaz H. F. and Hardy D. R. (2009) Recent changes in freezing level heights in the Tropics with implications for the deglacierization of high mountain regions. *Geophys. Res. Lett.* **36**, L17701.

Bromley G. R. M., Hall B. L., Stone J. O., Conway H. and Todd C. E. (2010) Late Cenozoic deposits at Reedy Glacier, Transantarctic Mountains: implications for former thickness of the West Antarctic Ice Sheet. *Quat. Sci. Rev.* **29**, 384–398.

Brook E. J. and Kurz M. D. (1993) Surface-exposure chronology using in situ cosmogenic ^{3}He in Antarctic quartz sandstone boulders. *Quat. Res.* **39**, 1–10.

Brook E. J., Kurz M. D., Ackert, Jr., R. P., Denton G. H., Brown E. T., Raisbeck G. M. and Yiou F. (1993) Chronology of Glacier advances in Arena Valley, Antarctica, using in situ cosmogenic ^{3}He and ^{10}Be. *Quat. Res.* **39**, 11–23.

Cassata W. S. and Renne P. R. (2013) Systematic variations of argon diffusion in feldspars and implications for thermochronometry. *Geochim. Cosmochim. Acta* **112**, 251–287.

Cerling T. E. (1990) Dating geomorphologic surfaces using cosmogenic ^{3}He. *Quat. Res.* **33**, 148–156.

Cherniak D. J., Watson E. B. and Thomas J. B. (2009) Diffusion of helium in zircon and apatite. *Chem. Geol.* **268**, 155–166.

Cherniak D. J., Thomas J. B. and Watson E. B. (2014) Neon diffusion in olivine and quartz. *Chem. Geol.* **371**, 68–82.

Clay P. L., Baxter E. F., Cherniak D. J., Kelley S. P., Thomas J. B. and Watson E. B. (2010) Two diffusion pathways in quartz: a combined UV-laser and RBS study. *Geochim. Cosmochim. Acta* **74**, 5906–5925.

Crank J. (1975) *The mathematics of diffusion*. Oxford University Press, London.

Dennen W. H. (1966) Stoichiometric substitution in natural quartz. *Geochim. Cosmochim. Acta* **30**, 1235–1241.

Dunai T. J., González López G. A. and Juez-Larré J. (2005) Oligocene–Miocene age of aridity in the Atacama Desert revealed by exposure dating of erosion-sensitive landforms. *Geology* **33**, 321.

Farley K. A., Shuster D. L., Watson E. B., Wanser K. H. and Balco G. (2010) Numerical investigations of apatite ^{4}He/^{3}He thermochronometry. *Geochem. Geophys. Geosyst.* **11**.

Fechtig H. and Kalbitzer S. (1966) The diffusion of argon in potassium-bearing solids. In *Potassium–Argon Dating* (eds. O. A. Schaeffer and J. Zahringer). Springer, Heidelberg, pp. 68–106.

Flowers R. M., Ketcham R. A., Shuster D. L. and Farley K. A. (2009) Apatite (U–Th)/He thermochronometry using a radiation damage accumulation and annealing model. *Geochim. Cosmochim. Acta* **73**, 2347–2365.

Goehring B. M., Kurz M. D., Balco G., Schaefer J. M., Licciardi J. and Lifton N. (2010) A reevaluation of in situ cosmogenic ^{3}He production rates. *Quat. Geochronol.* **5**, 410–418.

Götze J. (2009) Chemistry, textures and physical properties of quartz – geological interpretation and technical application. *Mineral. Mag.* **73**, 645–671.

Götze J., Plötze M., Graupner T., Hallbauer D. K. and Bray C. J. (2004) Trace element incorporation into quartz: a combined study by ICP-MS, electron spin resonance, cathodoluminescence, capillary ion analysis, and gas chromatography. *Geochim. Cosmochim. Acta* **68**, 3741–3759.

Gourbet L., Shuster D. L., Balco G., Cassata W. S., Renne P. R. and Rood D. (2012) Neon diffusion kinetics in olivine, pyroxene and feldspar: retentivity of cosmogenic and nucleogenic neon. *Geochim. Cosmochim. Acta* **86**, 21–36.

Granger D. E., Lifton N. A. and Willenbring J. K. (2013) A cosmic trip: 25 years of cosmogenic nuclides in geology. *Geol. Soc. Am. Bull.* **125**, 1379–1402.

Guenthner W. R., Reiners P. W., Ketcham R. A., Nasdala L. and Giester G. (2013) Helium diffusion in natural zircon: radiation damage, anisotropy, and the interpretation of zircon (U–Th)/He thermochronology. *Am. J. Sci.* **313**, 145–198.

Heaney P. J. and Veblen D. R. (1991) Observations of the a–b phase transition in quartz: a review of imaging and diffraction studies and some new results. *Am. Mineral.* **76**, 1018–1032.

Hetzel R., Niedermann S., Tao M., Kubik P. W., Ivy-Ochs S., Gao B. and Strecker M. R. (2002) Low slip rates and long-term preservation of geomorphic features in Central Asia. *Nature* **417**, 428–432.

Kelly M. A., Lowell T. V., Applegate P. J., Smith C. A., Phillips F. M. and Hudson A. M. (2012) Late glacial fluctuations of Quelccaya Ice Cap, southeastern Peru. *Geology* **40**, 991–994.

Kelly M. A., Lowell T. V., Applegate P. J., Phillips F. M., Schaefer J. M., Smith C. A., Kim H., Leonard K. C. and Hudson A. M. (2013) A locally calibrated, late glacial ^{10}Be production rate from a low-latitude, high-altitude site in the Peruvian Andes. *Quat. Geochronol.*, 1–16.

Kober F., Ivy-Ochs S., Schlunegger F., Baur H., Kubik P. W. and Wieler R. (2007) Denudation rates and a topography-driven rainfall threshold in northern Chile: multiple cosmogenic nuclide data and sediment yield budgets. *Geomorphology* **83**, 97–120.

Kober F., Alfimov V., Ivy-Ochs S., Kubik P. W. and Wieler R. (2011) The cosmogenic ^{21}Ne production rate in quartz evaluated on a large set of existing ^{21}Ne–^{10}Be data. *Earth Planet. Sci. Lett.* **302**, 163–171.

Krickl R., Nasdala L., Götze J., Grambole D. and Wirth R. (2008) Alpha-irradiation effects in SiO_2. *Eur. J. Mineral.* **20**, 517–522.

Lifton N., Sato T. and Dunai T. J. (2014) Scaling in situ cosmogenic nuclide production rates using analytical approximations to atmospheric cosmic-ray fluxes. *Earth Planet. Sci. Lett.* **386**, 149–160.

Lovera O. M., Richter F. M. and Harrison T. M. (1989) The ^{40}Ar/^{39}Ar thermochronometry for slowly cooled samples having a distribution of diffusion domain sizes. *J. Geophys. Res.* **94**, 17917–17935.

Lovera O. M., Grove M., Harrison T. M. and Mahon K. I. (1997) Systematic analysis of K-feldspar ^{40}Ar/^{39}Ar step heating results: I. Significance of activation energy determinations. *Geochim. Cosmochim. Acta* **61**, 3171–3192.

Masarik, J. and Reedy R. C. (1995a) Monte Carlo simulation of in-situ produced cosmogenic nuclides. *Secul. Var. Cosmogenic Nuclide Prod. Work. St. Fe, NM, USA*.

Masarik J. and Reedy R. C. (1995b) Terrestrial cosmogenic-nuclide production systematics calculated from numerical simulations. *Earth Planet. Sci. Lett.* **136**, 381–395.

Meesters A. G. C. A. and Dunai T. J. (2002) Solving the production–diffusion equation for finite diffusion domains of various shapes: Part II. Application to cases with α-ejection and nonhomogeneous distribution of the source. *Chem. Geol.* **186**, 57–73.

Müller A., Wiedenbeck M., van den Kerkhof A. M., Kronz A. and Simon K. (2003) Trace elements in quartz – a combined electron microprobe, secondary ion mass spectrometry, laser-ablation ICP-MS, and cathodoluminescence study. *Eur. J. Mineral.* **15**, 747–763.

Niedermann S. (2000) The ^{21}Ne production rate in quartz revisited. *Earth Planet. Sci. Lett.* **183**, 361–364.

Niedermann S., Graf T. and Marti K. (1993) Mass spectrometric identification of cosmic-ray-produced neon in terrestrial rocks with multiple neon components. *Earth Planet. Sci. Lett.* **118**, 65–73.

Niedermann S., Graf T., Kim J. S., Kohl C. P., Marti K. and Nishiizumi K. (1994) Cosmic-ray-produced ^{21}Ne in terrestrial quartz: the neon inventory of Sierra Nevada quartz separates. *Earth Planet. Sci. Lett.* **125**, 341–355.

Reich M., Ewing R. C., Ehlers T. a. and Becker U. (2007) Low-temperature anisotropic diffusion of helium in zircon: implications for zircon (U–Th)/He thermochronometry. *Geochim. Cosmochim. Acta* **71**, 3119–3130.

Saadoune I., Purton J. A. and de Leeuw N. H. (2009) He incorporation and diffusion pathways in pure and defective zircon $ZrSiO_4$: a density functional theory study. *Chem. Geol.* **258**, 182–196.

Sasnett P., Goehring B. M., Christie-Blick N. and Schaefer J. M. (2012) Do phreatomagmatic eruptions at Ubehebe Crater (Death Valley, California) relate to a wetter than present hydro-climate? *Geophys. Res. Lett.* **39**, L02401.

Shuster D. L. and Farley K. A. (2005) Diffusion kinetics of proton-induced ^{21}Ne, ^{3}He, and ^{4}He in quartz. *Geochim. Cosmochim. Acta* **69**, 2349–2359.

Shuster D. L. and Farley K. A. (2009) The influence of artificial radiation damage and thermal annealing on helium diffusion kinetics in apatite. *Geochim. Cosmochim. Acta* **73**, 183–196.

Shuster D. L., Farley K. A., Sisterson J. M. and Burnett D. S. (2004) Quantifying the diffusion kinetics and spatial distributions of radiogenic ^{4}He in minerals containing proton-induced ^{3}He. *Earth Planet. Sci. Lett.* **217**, 19–32.

Shuster D. L., Flowers R. M. and Farley K. A. (2006) The influence of natural radiation damage on helium diffusion kinetics in apatite. *Earth Planet. Sci. Lett.* **249**, 148–161.

Stone J. O. (2000) Air pressure and cosmogenic isotope production. *J. Geophys. Res.* **105**, 753–759.

Thompson L. G., Mosley-Thompson E., Davis M. E., Lin P. N., Henderson K. A., Cole-Dai J., Bolzan J. F. and Liu K. B. (1995) Late glacial station and Holocene tropical ice core records form Huascaran, Peru. *Science* **269**, 46–50.

Tremblay M. M., Shuster D. L. and Balco G. (2014) Cosmogenic noble gas paleothermometry. *Earth Planet. Sci. Lett.* **400**, 195–205.

Trull T. W., Kurz M. D. and Jenkins W. J. (1991) Diffusion of cosmogenic ^{3}He in olivine and quartz: implications for surface exposure dating. *Earth Planet. Sci. Lett.* **103**, 241–256.

Trull T., Brown E., Marty B., Raisbeck G. and Yiou F. (1995) Cosmogenic ^{10}Be and ^{3}He accumulation in Pleistocene beach terraces in Death Valley, California, USA: implications for cosmic-ray exposure dating of young surfaces in hot climates. *Chem. Geol.* **119**, 191–207.

Vermeesch P., Baur H., Heber V. S., Kober F., Oberholzer P., Schaefer J. M., Schlüchter C., Strasky S. and Wieler R. (2009) Cosmogenic ^{3}He and ^{21}Ne measured in quartz targets after one year of exposure in the Swiss Alps. *Earth Planet. Sci. Lett.* **284**, 417–425.

Watson E. B. and Cherniak D. J. (2003) Lattice diffusion of Ar in quartz, with constraints on Ar solubility and evidence of nanopores. *Geochim. Cosmochim. Acta* **67**, 2043–2062.

Weil J. A. (1992) A review of the EPR spectroscopy of the point defects in α-quartz: the decade 1982–1992. In *The Physics and Chemistry of SiO2 and the Si–SiO2 Interface*, vol. 2 (eds. C. R. Helms and B. E. Deal). Plenum Press, New York, pp. 131–144.

Wolf R. A., Farley K. A. and Kass D. M. (1998) Modeling of the temperature sensitivity of the apatite (U–Th)/He thermochronometer. *Chem. Geol.* **148**, 105–114.

Associate editor: Thure E. Cerling